THESIS FOR THE DEGREE OF LICENTIATE OF PHILOSOPHY

Local structure and dynamics in proton conducting perovskite oxides:

insights from quasielastic neutron scattering and infrared spectroscopy

Elena Naumovska

Department of Chemistry and Chemical Engineering
CHALMERS UNIVERSITY OF TECHNOLOGY
Göteborg, Sweden 2023

Local structure and dynamics in proton conducting perovskite oxides: insights from quasielastic neutron scattering and infrared spectroscopy

Elena Naumovska

Licentiatuppsatser vid Institutionen för kemi och kemiteknik
Chalmers tekniska högskola.
Nr 2023:17

Department of Chemistry and Chemical Engineering
Chalmers University of Technology
SE-41296 Göteborg, Sweden

Printed by Chalmers Digitaltryck
Göteborg, Sweden 2023

Elena Naumovska
Department of Chemistry and Chemical Engineering
Chalmers University of Technology

Abstract

Proton conducting oxides have been extensively studied in the past decade due to their potential application in a number of energy related devices such as solid oxide fuel cells, hydrogen sensors, and steam electrolyzers. However, the final industrialisation of these materials depends on unlocking fundamental questions about the relationship between their atomic structure, localized proton dynamics and proton conductivity. The aim of this thesis is to gather insights into these properties in proton conducting oxides based on the perovskite and perovskite-like brownmillerite structures, i.e., $BaZr_{1-x}Sc_xO_{3-x/2}$ with x = 0.10–0.65, and $Ba_2In_{1.85}M_{0.15}O_5$ with M = In, Ga, Sc and Y, as both powder samples and films. The investigations are experimental in nature and the main techniques used are quasielastic neutron scattering and infrared spectroscopy.

The studies of powder samples of $BaZr_{1-x}Sc_xO_{3-x/2}$ ($x = 0.10$ and 0.50) focused on exploring the nature of localised proton dynamics and how it depends on Sc dopant level *via* quasielastic neutron scattering. The results confirm earlier studies in which the localised proton dynamics can be described as proton transfers between neighboring oxygens and –OH reorientation motions. Both processes are found to exhibit a relaxation time and activation energy of the order of 1–10 picoseconds and some tens of meV, respectively, and it is found that these values depend insignificantly on the Sc dopant levels as investigated here. Films of $BaZr_{1-x}Sc_xO_{3-x/2}$, (x = 0.45, 0.54, and 0.65) were investigated with the aim to reveal possible differences in local structure to the corresponding powder samples. These investigations were performed using infrared spectroscopy. Analysis of the infrared spectra focused on the O–H stretch region (2000–3700 cm^{-1}) and revealed the presence of several distinct O–H stretch bands with unsystematic intensity and frequency in terms of Sc dopant level. For $x = 0.45$, the O–H stretch region was characterized by a broad, weak band between 2500 and 3700 cm^{-1}, suggesting the presence of a wide range of local surroundings of the protons in the material. The O–H stretch regions for x = 0.54 and 0.65 were characterised with a distinct, highly intense band centered at around 3400–3500 cm^{-1}, pointing towards relatively symmetric, weakly hydrogen-bonding, proton configurations. A comparison to the infrared spectra of powder samples of similar compositions suggests a more homogeneous distribution of proton sites in the powder samples compared to the films.

The studies on $Ba_2In_{1.85}M_{0.15}O_5$ with M = In, Ga, Sc and Y, focused on the relationship between localised proton dynamics and the type of dopant atom in powder samples, using quasielastic neutron scattering. Since before, it was known that the crystal structure of $Ba_2In_2O_6H_2$ is built up of cubic and "pseudo-cubic" layers of InO_6 octahedra, with two main types of proton sites, H(1) and H(2), present. Analysis of the quasielastic neutron scattering data reveals the presence of dynamics on the picosecond timescale, associated with proton transfer and/or –OH rotational motions of H(1) and H(2) protons, respectively, for temperatures above 400 K, quite independent on M. For dopants with significantly different ionic radii compared to In, i.e., M = Ga and Y, the combined analysis of the infrared spectra and quasielastic neutron scattering data suggests a larger fraction of protons on the H(2) site, as opposed to M = Sc and In, where there is a larger fraction of protons on the H(1) site. Analysis of the quasielastic neutron scattering data also revealed that doping with M = Ga, Sc and Y resulted in the presence of an additional proton site H(3) at temperatures above 450 K, which feature more complex dynamics, in accordance with a previous study on $Ba_2In_2O_6H_2$.

Keywords: *Perovskites, quasielastic neutron scattering, proton dynamics, proton- conducting oxides, infrared spectroscopy.*

List of publications

This thesis is based on the following publications:

I Localized proton motions in the proton conducting perovskites $BaZr_{1-x}Sc_x O_3H_x$ (x = 0.10 and 0.50) investigated with quasielastic neutron scattering
E. Naumovska, J. Orstadius, A. Perrichon, R. Lavén, M. M. Koza, and M. Karlsson
Under review

II Proton dynamics of brownmillerite $Ba_2In_{1.85}M_{0.15}O_5$ with M = In, Ga, Sc and Y based proton conductors investigated with quasielastic neutron scattering
E. Naumovska, A. Perrichon, F. Piccinelli, N. Jalarvo, and M. Karlsson
In Manuscript

III Local structure of hydrated nanocrystalline films of the proton conductor $BaZr_{1-x}Sc_xO_{3-x/2}$ studied by infrared spectroscopy
E. Naumovska, G. K. Nzulu, L. Mazzei, A. le Febvrier, K. Komander, M. Magnuson, M. Wolff, P. Eklund, and M. Karlsson
Under review

Related publications not included in the thesis:

Growth and thermal stability of Sc-doped $BaZrO_3$ thin films deposited on single crystal substrates
G. K. Nzulu, E. Naumovska, M. Karlsson, P. Eklund, M. Magnuson, A. le Febvrier,
Thin Solid Films 772 (2023) 139803

Contribution report

My contributions to the included papers:

I I was the main responsible for the analysis of the experimental data. I was the main responsible for writing the manuscript. The data collection was performed by Johannes Orstadius as part of his Masters thesis. The samples were synthesised and characterised by collaborators at Chalmers University of Technology.

II I contributed to the planning of the QENS experiments and I was the main responsible for the data collection and analysis of the experimental data. I was the main responsible for writing the paper. The experiment was performed remotely due to travel restrictions imposed by the COVID pandemic. The samples were synthesised and characterised by collaborators at University of Verona.

III I contributed to the planning and execution of the experiments and I was the main responsible for the experimental data collection and analysis of the experimental data. I was the main responsible for writing the manuscript. The samples were synthesised and characterised by collaborators at Linköping University.

To my grandparents Dr. Milorad Mladenovic & Dr. Leposava Mladenovic
Semper amati, semper desiderati.
Primum non nocere...

Contents

List of abbreviations

BZO	Barium zirconate
BIO	Barium indate
EISF	Elastic incoherent structure factor
FWHM	Full width at half maximum
IR	Infrared
ILL	Institut Laue-Langevin
MD	Molecular dynamics
NRA	Nuclear reaction analysis
QENS	Quasielastic neutron scattering
SNS	Spallation neutron source
TGA	Thermogravimetric analysis
TOF	Time-of-flight

CHAPTER 1

Towards a green energy transition

> I believe that water will one day be employed as fuel,..., that will furnish an inexhaustible source of heat and light.
>
> *Jules Verne*

The ongoing climate crisis, the demand for lowering gas emissions (e.g. CO_2) and the COVID-19 pandemic have served as catalysts for developing technologies which can promote the green energy transition to a more environmental and sustainable society. "Green energy devices" produce close to zero greenhouse gas emissions during generation of electricity, compared to fossil fuels, which are the biggest source of CO_2 emissions that are ultimately responsible for trapping heat at the Earth's atmosphere that leads to climate change and global warming [1]; examples of such devices are solar panels, which are able to produce electricity from sunlight with no emissions, and wind turbines, which manage to generate power from wind without fossil burning, and water turbines which generate electricity from water, and fuel cells which manage to produce electricity with (clean) water as side product [2, 3]. Losing fossil fuels dependence and achieving a transition to "green energy" can likewise tremendously contribute to preserving natural resources, the biodiversity and ecosystem, all of which are threatened when extracting and transporting fossil fuels [1]. This is especially important as recent report pointed out that six out of the nine planetary boundaries that are crucial for maintaining the stability and resilience of the Earth system are transgressed by human activities [4]. In order to implement this transition, however, it is important to design and optimise materials for their final applications in "green energy devices". These materials should be functional, i.e., they should generate maximal energy while at the same time being cheap to produce and be non-toxic to the environment and finally be able to impact the energy generation and contribute to bigger energy savings [5].

If we see from a material point of view, perhaps one of the most studied and explored materials for renewable energy devices are the perovskite class of materials with ABO_3 and perovskite-like brownmillerite $A_2B_2O_5$ type structures, where A and B are two cations, usually with significantly different sizes and O is oxygen. A particularly important perovskite material is $BaZrO_3$, due to its wide range of unique properties (often when doped with acceptor dopants e.g. Y, In, Sc, Eu, etc. to the Zr site), such as proton conductivity, photoluminescence, as well as electronic and magnetic properties; similarly, the brownmillerite $Ba_2In_2O_5$ is particularly important due to its anionic and proton conductivity [6–11]. These ion-conducting properties make them of interest for application in devices such as hydrogen sensors, fuel cells, hydrogen separation membranes, steam electrolyzers, and membrane reactors to name a few [12–17]. Among these, fuel cells are considered a particularly

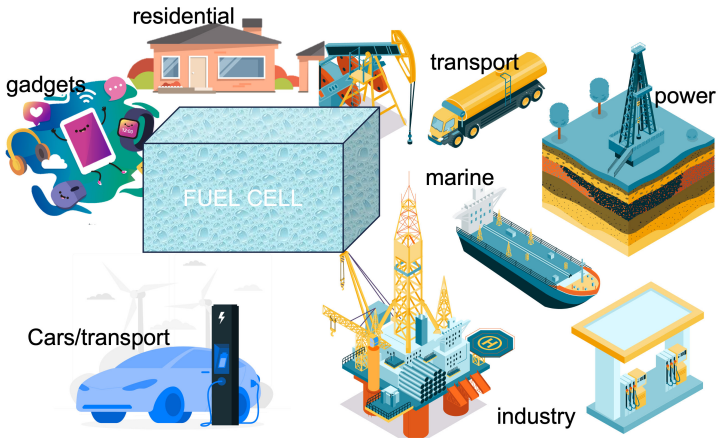

Figure 1.1: Illustration of a smart city with fuel cells being used for primary and backup power of residential and industrial buildings, and power of vehicles and gadgets. Designed by Freepik, slidesgo/Freepik, and macrovector/Freepik.

promising green alternative for electricity generation in a non-polluting way, with a number of applications based on fuel cells developed so far (Figure 1.1).

Currently, a specific challenge in the fuel cell field is to design proton conducting fuel cells operating in the intermediate temperature range of 200–400 °C; for an overview of different fuel cell technologies see Appendix A. Nowadays, apart from the classical experimental and theoretical research, scientists apply various artificial intelligence models for more precise predictions and simulations, enhancing the practicality of the potential material candidates [12]. Despite the challenges in the design and optimisation of these materials (e.g. synthesis suitable for industrial purposes, cheap materials, and significantly high performance like high proton conductivity) the research in the field of perovskite proton conductors is still progressing for almost half a century now [12, 18, 19]. And while there is an enormous progress that has led to the industrialisation of some materials, the journey of finding the ideal material which will revolutionise the field (in terms of fabrication, stability and efficiency of devices) of fuel cells continues [12]. Ongoing studies, however, aim to expand the research on materials beyond perovskite-based proton conductors with hopes to include a broader range of materials that can improve the working conditions of the fuel cell while at the same time also broaden the applicability to other devices such as hydrogen sensors, separation membranes or electorlyzers as well [12, 18, 20–22].

Motivated by the current need for developing new, better performing proton conducting perovskites for application in intermediate temperature fuel cells, this thesis focuses on investigations of structure and dynamics in some particularly important proton conducting perovskite materials, specifically Sc doped $BaZrO_3$ and perovskite-like brownmillerite type $Ba_2In_{1.85}M_{0.15}O_5$ (M = In, Ga, Sc and Y). The research has been experimental in nature and the primary tools to this end have been quasielastic neutron scattering and infrared spectroscopy. The current results presented further in this thesis, provide new insights into the fundamental properties related to both local structure and dynamics of Sc doped $BaZrO_3$ systems which may contribute to the development of these materials for their ultimate application in intermediate temperature solid oxide fuel cells. Similarly, the results on $Ba_2In_{1.85}M_{0.15}O_5$ (M = In, Ga, Sc and Y) give new insights regarding the relationship between the type of dopant atom and local proton dynamics. A more detailed description about the studied materials and of the wider field of proton conducting oxides is presented in Chapter 2.

CHAPTER 2

Proton conducting Oxides

> To comprehend hydrogen is to see all material science.
>
> *Victor Frederick Weisskopf*

2.1 Proton conducting oxides – retrospective over the last decades

Proton conductivity in solids has been an attractive topic of interest in material science ever since the discovery of proton conductivity in ice in Japan more than one century ago [23]. From a historical point of view, the first appearance of proton conductivity in the literature is even older, from 1806, when de Grotthus reported on the existence of protons in aqueous solutions [24]. In the 1960s already, the proton conducting perfluorosulfonic acid polymer, nowadays known as Nafion, was applied as a proton conducting membrane for the very first time and was used for the Gemini and Apollo space programs as fuel cell electrolyte operating at temperatures below 100 °C [23]. This significant moment in the field of proton conducting solids was followed by several reports on different inorganic proton conductors with high conductivity for temperatures below 200 °C [23, 25–27]. The first report on high temperature proton conducting oxides operating between 800 to 1000 °C, on the other hand, was published by Iwahara and coworkers in the 1980s marking yet another important moment in this field [28].

Even now, almost half a century later, the field of proton conducting oxides continues to be an intriguing research topic mostly due to the demand of "green energy devices" which would eventually serve as a catalyst for the world's green energy transition. As can be seen in Figure 2.1, the annual number of publications related to proton conducting oxides remains high and quite constant over the past decade, which proves that proton conducting oxides remain a thriving topic of research. The research on proton conducting oxides in particular focuses on structural and mechanistic features of material candidates primarily for applications in solid oxide fuel cell technology which is believed to be one of the key players for the energy transition. These efforts are motivated by not only discoveries of novel materials, but also curiosity to develop a fundamental understanding for how these materials work, advances in experimental approaches and application of artificial intelligence and machine learning [12].

In the past decade the field of solid proton conductors has been governed by progress in the discovery of new materials, as well as developing a better understanding of the mechanism of proton

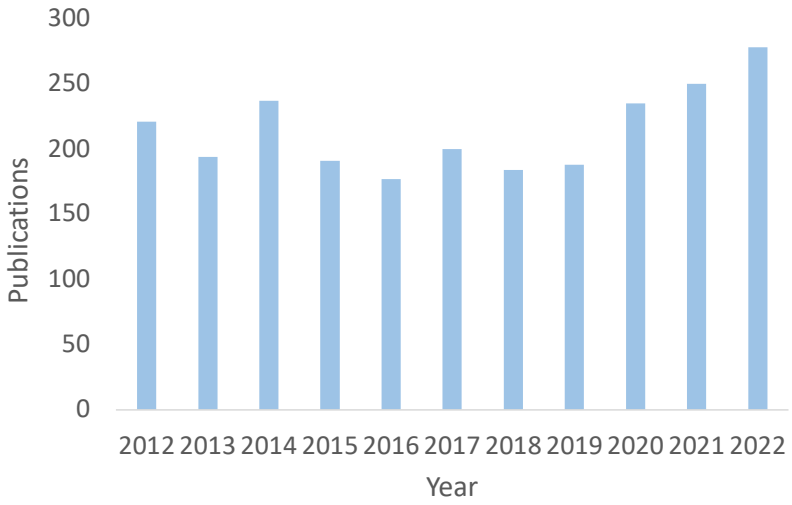

Figure 2.1: Number of publications related to proton conducting oxides over the last decade as per Scopus. Key words searched: proton conducting oxides.

conductivity and its connection to the structural and dynamical properties of materials [11, 22, 29, 30]. To be used in a fuel cell, the conductivity needs to be at least 10^{-2} S/cm [31].

In more detail, the studies on perovskite and perovskite-like proton conducting oxides have primarily focused on elucidating the relationship between the macroscopic proton conductivity and how it is affected by the type and concentration of dopant atoms. Importantly, it has been established that the type of dopant atom and doping concentration have significant influence on the proton conductivity [10, 23, 32–44, 44, 45, 45–48]. For example, for $BaCeO_3$ based materials, doping 10–15% with Y on the Ce site was shown to give a maximal proton conductivity in the range of 0.01 and 0.12 S/cm at temperatures between 500 °C and 600 °C [36–39]. For $BaZrO_3$, doping with 10–20% of Y on the Zr site corresponds to highest proton conductivity in the range between 10^{-3} and $3.3{\cdot}10^{-2}$ S/cm [49–51]. In comparison, the brownmillerite $Ba_2In_2O_5$ exhibits a proton conductivity between 10^{-6} and 10^{-5} S/cm at temperatures between 400 °C and 500 °C [52, 53]. Doping $Ba_2In_2O_5$ with 20% Yb on the In site results in an increased proton conductivity to $1.7{\cdot}10^{-3}$ S/cm [54].

Figure 2.2 shows the conductivity of the best performing proton conducting perovskite along with some of the best materials used in low and high temperature fuel cells respectively. It can be seen that there is a "gap" or a lack of materials with conductivity larger than 10^{-2} S/cm at the targeted intermediate temperature range between 150 °C and 450 °C [31]. The most promising materials that can potentially fill in this gap are based on $BaZrO_3$, $BaCeO_3$ and $Ba_2In_2O_5$ [55]. However, before they can do so, their proton conductivity needs to be, rationally, increased to at least 10^{-2} S/cm in the temperature range of interest. Such a rational increase in proton conductivity depends on a better understanding of structure-conductivity relationships in the most promising materials, since by understanding how the nature of the structure affects proton conduction one should be able to propose materials with specific structures to achieve higher proton conductivity.

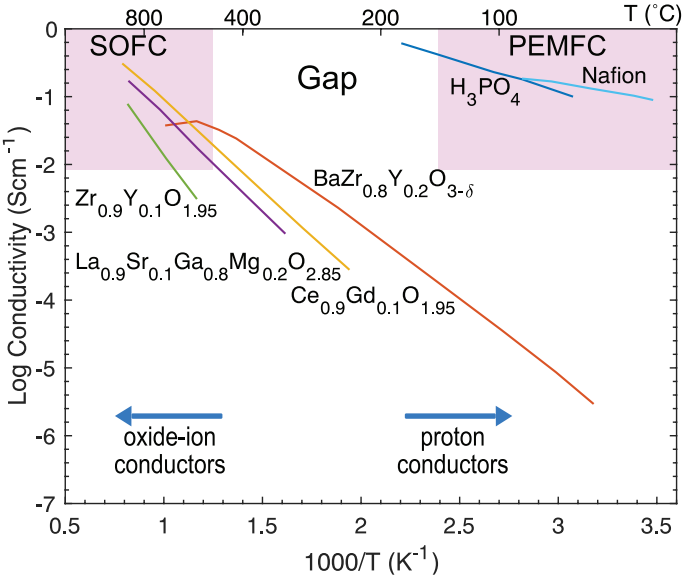

Figure 2.2: Ionic conductivity of some of the best ionic conductors together with the operation ranges of low temperature proton-exchange membrane fuel cells (PEMs) and high temperature solid oxide fuel cells (SOFCs) (pink), respectively. The figure is modified as per data from [56].

2.2 Perovskite ABO_3-based materials

Acceptor-doped perovskite type oxides based on $BaZrO_3$ and $BaCeO_3$,[1] of the general formula $BaM'_{1-x}M''_xO_{3-x/2}$ ($M' = Zr^{4+}$ or Ce^{4+}; M'' = trivalent cation such as Sc, In, Y; $0 < x < 1$), are highly attractive as proton conducting electrolytes for various electrochemical devices due to their high proton conductivity (see Figure 2.2) and chemical stability at intermediate temperatures between 150 °C and 450 °C, which is why they are perhaps one of the most studied classes of proton conducting oxides [13–16, 57–62].

Synthesis of polycrystalline powder samples of these materials may be achieved by solid state synthesis. In this synthesis route precursos are first mixed and ground to obtain a homogenous powder mixture. Thereafter, this powder mixture is compressed into a pellet which is exposed to high temperatures between 1200 °C and 2000 °C at which the prescursors react to obtain the desired end product. The high temperature required for synthesis is an important issue that complicates further industrialisation of these systems as the high temperature is not suitable for industrial purposes, mostly from an economical point of view [33, 63, 64]. Furthermore, the high temperature synthesis may lead to other problems, such as Ba deficiency, which can result in the formation of grain boundaries with low proton conductivity [65]. Other synthesis methods such as sol-gel (obtaining solids from small molecules that undergo irreversible chemical reactions) or the wet approach (obtaining solids from chemical reactions in solutions) have been designed to lower the synthesis temperature below 100 °C and/or to obtain a high amount of samples with less grain boundaries [66]. However, organic traces present in the proton conducting oxide materials as a result of these synthesis methods, can cause problems when using neutron scattering techniques, as

[1]Doping with trivalent atoms on the Zr/Ce site is required for formation of oxygen vacancies that are needed for proton incorporation.

this technique is highly sensitive to such species.

The synthesis of polycrystalline or epitaxial/single crystal films of proton conducting oxides with thickness in the nm range is normally done with physical vapour deposition (PVD).[2] Sputtering is a PVD-based technique which can yield films with a thickness up to several μm [67, 68].

While the synthesis methods described above result in products essentially free from protons, protons can be introduced into the materials following a hydration procedure. Hydration of the samples is usually performed by heating the samples to 500–700 °C in a furnace subjected by a water vapour flow, and followed by slow cooling to ambient temperatures. For the purpose of this study, the hydrated samples of Sc-doped $BaZrO_3$ powder and film samples were prepared by annealing as-prepared powders and films in a tube furnace subjected to a nitrogen flow with water vapor, while cooling from 600 to 200 °C at a rate of 0.2 °C/min. A schematic drawing of acceptor doping and proton incorporation is presented in Figure 2.3. For further details related to incorporation of protons, see Appendix B.

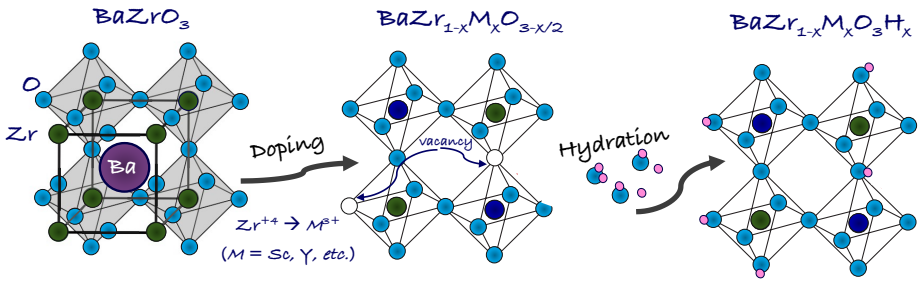

Figure 2.3: Schematic drawing of acceptor doping and proton incorporation in $BaZrO_3$. Doping with trivalent atoms creates oxygen vacancies; upon hydration the water dissociates into hydroxyl groups which fill the oxygen vacancies and protons are incorporated in the structure.

2.2.1 Proton mobility

The nature of proton conduction in proton conducting oxides has been extensively studied from both theoretical and experimental point of views, however, fundamentals regarding the proton motion and how it is affected by structural properties such as the type and concentration of dopant atoms are not yet fully understood [10, 29, 69, 70].

Theoretically, molecular dynamics (MD) simulations of a proton in $BaCeO_3$ showed that the proton conduction mechanism may be divided into two elementary, short-range (localized), dynamic processes, namely proton transfer between two adjacent oxygens, and rotational diffusion of the proton around a specific oxygen (see Figure 2.4), whereas the long-range translation of protons occurs as a series of such processes [71].

Experimentally, proton motion in acceptor doped perovskites have been mostly studied using neutron scattering techniques [72], which are generally in agreement with theoretical results [73–79]. Because of the bond breaking needed for the proton to transfer (jump) from one oxygen and attach to another, the proton transfer is usually considered to be the rate-limiting process [74, 80–82]. However, since it has been difficult to separate the contributions from proton transfer and O-H

[2]PVD is a deposition method where the atoms of a target material are vaporised from a solid source and condensed on a substrate.

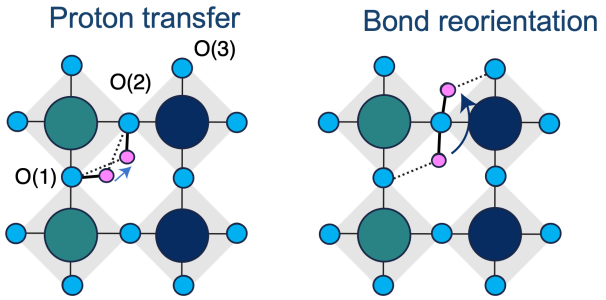

Figure 2.4: Schematic drawing of proton transfer and proton reorientation for an acceptor doped perovskite (ab plane). Note that O(1) and O(2) are examples of two neighbouring oxygens.

rotational diffusion in the analysis of experimental data, no mutual understanding has been reached so far [76, 77]. In more detail, it has been found that the proton mobility is strongly influenced by structural and chemical distortions introduced with dopant atoms, although the actual reason for this is still unclear [83–86]. Hempelmann introduced the idea that the dopants change the coordination environment of the oxygens, which results in protons spending longer time at each oxygen before migrating away [73]. Furthermore, a recent study on $BaZr_{0.5}In_{0.5}O_{2.75}$ showed that additional proton sites that contribute to a decreased number of immobile protons when increasing the doping concentration of In to 50% [83]. Interestingly, no additional proton sites were observed for 50% doping with Sc as per the same study [83].

2.3 Brownmillerite $A_2B_2O_5$-based materials

The brownmillerite structure, such as of $Ba_2In_2O_5$, is composed of InO_6 octahedral layers and InO_4 tetrahedral layers, and Ba atoms in between and oxygen vacancies arranged along the [0 1 0] direction as shown in Figure 2.5. The brownmillerite $Ba_2In_2O_5$ transforms into $Ba_2In_2O_5(H_2O)_x$ upon hydration. Here x can be between 0 (dehydrated) and 1 (fully hydrated phase), depending on the hydration conditions. During hydration the water dissociates into hydroxyl groups which fill the tetrahedral layers and distort them thus creating pesudo-cubic phases, see Figure 2.5. The protons migrate into the not significantly distorted, cubic layers [87–89].

Various doping strategies have been proposed for stabilisation of the tetrahedral and cubic structures of $Ba_2In_2O_5$. For example, some studies showed that doping with P and S on the In site of $Ba_2In_2O_5$ results in stabilisation of the cubic layer [91, 92]. Several computational and experimental studies in the last decade concluded that there are (at least) two proton sites for $Ba_2In_2O_5(H_2O)_x$, as seen in Figure 2.6 [87, 88, 93–95]. In the first proton site [H(1)] the protons are covalently bonded to oxygen atoms which connect the two layers and have hydrogen bonds with either an oxygen from the cubic or pseudo-cubic layers. Recent studies concluded that in the fully-hydrated $Ba_2In_2O_5$, H(1) is in fact divided in a way that the majority of protons form strong hydrogen bonds with oxygens from the cubic layer, whereas the rest of the protons form weak hydrogen bonds with oxygens from the pseudo-cubic layer [90]. The second proton site, [H(2)] in turn, is characterised with protons covalently bonding to oxygens from the pseudo-cubic layer of a neighbouring octahedra, with a bond angle of almost 180°, see Figure 2.6.

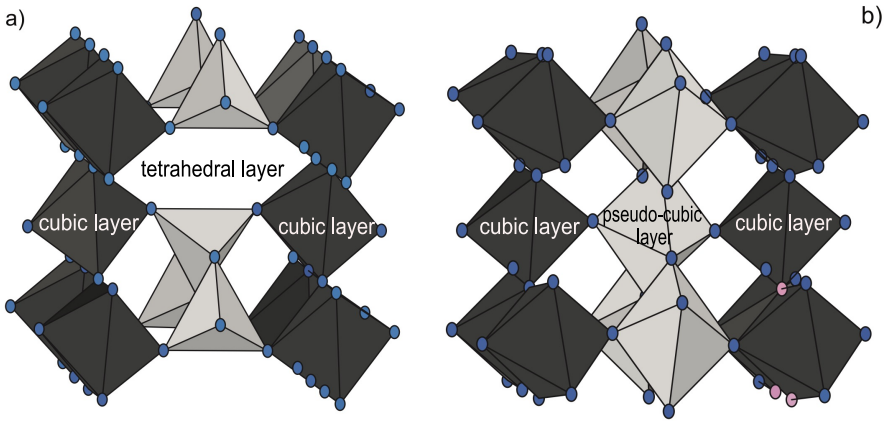

Figure 2.5: Schematic drawing of the (a) dry and (b) hydrated $Ba_2In_2O_5$. Note that the oxygens are blue and hydrogen is pink. Adapted from [90].

2.3.1 Proton mobility

Similar as for the acceptor doped perovskites, the proton conducting mechanism of brownmillerites such as $Ba_2In_2O_6H_2$ may be divided into two localized motions, i.e., proton transfers from one to another neighbouring oxygen and reorientational motion around one oxygen [88].

In more detail, recent studies based on neutron spectroscopy techniques distinguished four dynamical processes (based on proton transfers and/or reorientation motions) present in $Ba_2In_2O_6H_2$ [90]. In the picosecond timescale (0.4–77 ps) Perrichon *et al.* observed three localized dynamical processes (*cf* Figure 2.6), one cosisted of reorientational motion of H(1) protons with low activation energy E_a = 19.3 meV in the range of 2.8–4.6 ps, other consisted of proton transfers of H(2) protons between neighbouring oxygens with E_a = 13.4 meV, in the range of 0.4–0.5 ps, and a third process consisted of a mixture of transfers and reorientational motions with (significantly higher) E_a = 35 meV, in the range of 45–77 ps. An additional, much slower process, in the nanosecond timescale, in the range of 1.2–6.6 ns, with higher activation energy (E_a = 184.9 meV), was interpreted as long range diffusion of protons [90].

Motivated by these studies and with the hope to unravel the mechanistic details of proton diffusivity especially, in regard to the nature of localised H(1) and H(2) dynamics and how it depends on the type of dopant atom, this thesis reports on a study of the proton dynamics in hydrated $Ba_2In_{1.85}M_{0.15}O_5$ with M = In, Ga, Sc and Y.

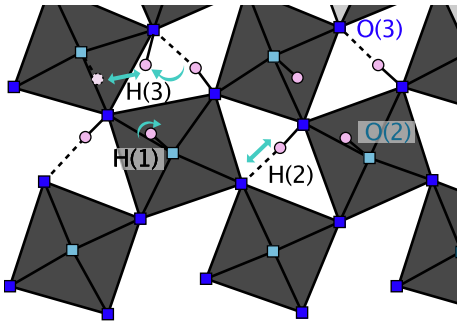

Figure 2.6: Schematic drawing of proton sites in hydrated $Ba_2In_2O_5$.

2.3.2 Concluding remarks and scope of thesis

As shown above, there has been a significant effort to design solid proton conductors beyond the perovskites, however, perovskite and brownmillerite structured materials still remain the most promising types of proton conducting oxides for eventual applications in energy related devices mostly because of their high conductivity and simple manufacturing process [1, 29, 33, 96]. This thesis aims to elucidate key questions related to local structure and proton dynamics in these materials, which can to some extent contribute to the development that leads to the fabrication of high performing intermediate temperature fuel cells. The studies have been focused on polycrystalline powder samples of $BaZr_{1-x}Sc_xO_{3-x/2}$ (x = 0.10 and 0.50) and $Ba_2In_{1.85}M_{0.15}O_5$ (M = In, Ga, Sc and Y), as well as of films of $BaZr_{1-x}Sc_xO_{3-x/2}$ (x = 0.45, 0.54, and 0.64). Sc has been chosen as a system model dopant atom because its ionic radius is close to the one of Zr, which results in a cubic structure with high doping concentration and high proton conductivity (as opposed to e.g. Y which is much larger than Zr and does not remain cubic for large doping concentrations). This implies that it is possible to study the local structure and dynamics over a large range of dopant concentrations with the overall crystal structure essentially being unaffected. The primary methods used for these investigations have been neutron scattering and infrared spectroscopy. A concise description of these and other methods used in this thesis is presented in the next chapter.

CHAPTER 3

Methodology

> It is a wild dance floor there at the molecular level.
>
> *Roald Hoffmann*

The beauty of experimental research lies in the combination of diverse techniques for studying the atomic structure and dynamics of materials. This thesis is primarily built on investigations using quasielastic neutron scattering (QENS) and infrared (IR) spectroscopy. In addition, thermogravimetric analysis (TGA) and nuclear reaction analysis (NRA) have been used. A brief description of the methods needed to understand their main features is presented below.

3.1 Neutron scattering

3.1.1 Foundation and mathematical background

Understanding the position and motion of atoms as well as their relationship to the overall structure of a material is an important topic in material science. While X-rays are employed as a routine "tool" for the measurement of crystal structure their disadvantage is their inability to detect light elements such as hydrogen, see Figure 3.1. On the other hand, neutrons can detect hydrogen.

Considering that the neutron is in fact a wave that has a sinusoidal oscillation in space and time, the square of that amplitude would give the probability of the neutron to be found at a certain location [97, 98]. In the event of neutron scattering, the neutron's amplitude is related to

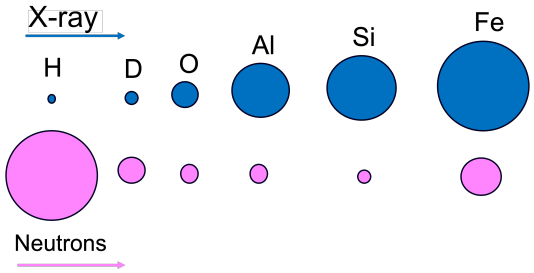

Figure 3.1: Schematic drawing of the X-ray and neutron cross-sections of some elements. Figure adapted from [97].

the strength of the interaction between the nucleus and the neutron itself, whereas the scattered neutron wave is isotropic[1] and can be written as $(-b/\vec{r})e^{ik\vec{r}}$, considering the nucleus is at the center of the coordination system [97, 98]. In this context, $\vec{k}$ is the wave vector of magnitude $\vec{k} = 2\pi/\lambda$, $\vec{r}$ is the position vector, b is the scattering length of the nucleus which gives us the strength of the neutron-nucleus interaction, $(1/\vec{r})$ is the factor used for the inverse square law which points out that the intensity of the neutron beam, defined by the square of the amplitude, is decreasing as the inverse square of the distance from the source. This type of collision occurs without any energy change of the neutron and is called elastic. However, when penetrating matter, the neutron can also change momentum and energy given that the scattering is occurring for atoms moving around (to some extent) and this type of scattering resulting in energy gain or loss is called inelastic. The amount of momentum transferred by the neutron during this type of collision is called momentum transfer and is described as $h/2\pi\vec{Q} = h/2\pi(\vec{k} - \vec{k'})$, where $\vec{k}$ is the incident wave vector at the neutron, and $\vec{k'}$ is the scattered wave vector. Accordingly, $\vec{Q} = \vec{k} - \vec{k'}$ is the scattering vector and can be geometrically represented by the scattering triangle shown in Fig 3.2. As can be seen, the direction and magnitude of Q is dependent on the incident and scattered neutrons (in terms of vector addition), as well as the 2θ angle named the scattering angle [97, 98]. The scattering length b, which is different for different atoms and different isotopes of atoms is connected to the cross section σ through $\sigma = 4\pi\bar{b^2}$ [97, 98].

Experimentally, the quantity that is measured in a neutron scattering experiment is given by the double differential cross-section according to:

$$\frac{d^2\sigma}{d\Omega dE_f} = \frac{k'}{k}\frac{1}{4\pi}\left\{\sigma_{coh}S_{coh}(Q,E) + \sigma_{inc}S_{inc}(Q,E)\right\} \tag{3.1}$$

where

$$\sigma_{coh} = 4\pi\langle b\rangle^2 = 4\pi b^2 \tag{3.2}$$

$$\sigma_{inc} = 4\pi(\langle b\rangle^2 - \langle b\rangle^2) \tag{3.3}$$

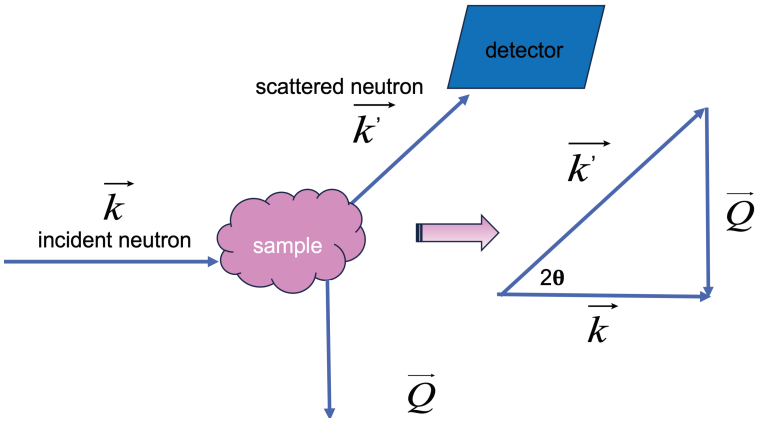

Figure 3.2: Schematic drawing of a scattering experiment along with the relations of incident and scattered wave vectors.

[1]The scattering event of the neutron can be described by the cross section σ quod est the effective area of the nucleus to the passing neutron. When the neutron hits this area, it scatters isotropically (it has an equal probability in any direction) because the nuclear potential range is much smaller than the neutron's wavelength.

Here, $S_{coh}(Q, E)$ and $S_{inc}(Q, E)$ are the coherent and incoherent dynamic structure factors, respectively, which contain information about correlations in both space and time, and σ_{coh} and σ_{inc} are the coherent and incoherent cross sections, respectively. Incoherent scattering arises when there is a random variability in the scattering lengths of the atoms in the sample, such as from different isotopes of the same element or isotopes with non-zero nuclear spin (such as hydrogen) and it gives information on the behaviour of single particles, as opposed to coherent scattering which provides information on spatial correlation or collective motion and thus answers questions related to atom positions [97, 98]. For hydrogen the coherent cross section $\sigma_{coh} = 1.76$ barn is rather small, whereas the incoherent cross section $\sigma_{inc} = 80.26$ barn is extraordinary large [98].[2] Furthermore, the scattering of the neutrons can be either elastic or inelastic. Elastic scattering provides information about atoms positions and their rearrangements. Inelastic scattering occurs when the neutrons undergo a change in energy at the scattering event, and it can give information about both diffusional and vibrational dynamics in a material. A subcategory of inelastic scattering is QENS, which occurs due to stochastic (non-periodic) motions of atoms, such as diffusion or molecular re-orientation (in a material). Such motions lead to small energy transfers of the neutrons which results in a continuous broadening of the elastic peak of the overall spectrum [97, 98]. A schematic drawing of the three scattering components, i.e. elastic, inelastic and quasielastic scattering, which may be measured in a neutron scattering experiment are presented in Figure 3.3.

3.1.2 Experimental considerations

The measured scattering intensity, $S(Q, E)$, in a QENS experiment, can be expressed as

$$S(Q, E)_{\text{meas}} \propto S(Q, E) \otimes R(Q, E), \tag{3.4}$$

where $S(Q, E)$ is the dynamic structure factor that contains information about the dynamical properties of the investigated material, and $R(Q, E)$ is the instrumental resolution function.

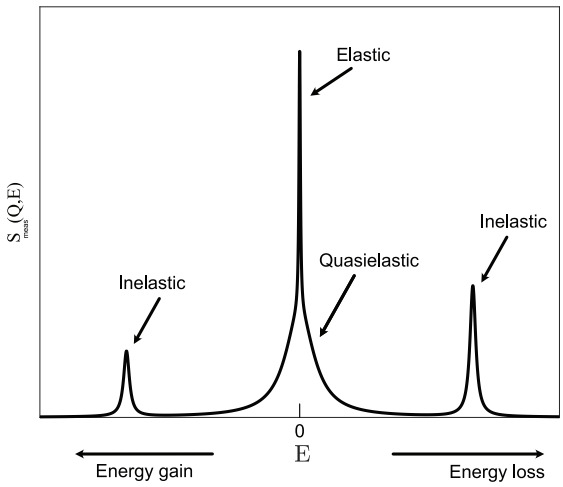

Figure 3.3: Schematic drawing of the elastic, inelastic and quasielastic scattering, which are measured in a neutron scattering experiment. The figure is taken from [99].

[2]Note that a metric unit of area equal to 10^{-28} m^2 = 1 barn.

While, usually, $S(Q,E)$ is comprised of one coherent and one incoherent part, previous QENS studies of proton conducting oxides showed that only incoherent scattering from the protons contributes to the quasielastic signal [72], which points out that the signal can be generally attributed to proton self-dynamics. For the QENS experiments in this thesis, $S(Q,E)$ was fitted with a function composed of one elastic component, described as the intensity $I_D(Q)$ multiplied with a Dirac delta function, a quasielastic component which represents the broadening of the elastic peak, as the intensity $I_L(Q)$ multiplied with a Lorentzian function $L(Q,E)$, and a background, bkg, see Eq. (3.5).

$$S(Q,E) = I_D(Q)\delta(E) + I_L(Q)L(Q,E) + bkg. \tag{3.5}$$

The background comes from scattering of species that move to fast to be detected and thus cause broadening of the QENS signal to the baseline, or inelastic scattering that forms peaks in the QENS signal. From the full width at half maximum (FWHM) of the Lorentzian function one can obtain information about the timescale (τ) of these processes as $\tau = 2\hbar/FWHM$, which are important for accessing more information about the nature of the localized motion and rate-limiting steps for long range diffusion, in our case. The activation energy can be obtained from the temperature dependence of FWHM assuming it follows an Arrhenius law. Figure 3.4, as an example, shows the $S(Q,E)$ for hydrated $BaZr_{0.50}Sc_{0.50}O_{2.75}$ together with fits featuring one Lorentzian function.

3.1.3 Analysis of the spatial geometry of the localised dynamics

Information regarding the spatial geometry of localised dynamics observed as quasielastic scattering can be obtained from analysis of the elastic incoherent structure factor (EISF), defined as the ratio of the elastic intensity over the sum of the elastic and quasielastic intensity (see Eq. 3.5), i.e. EISF $= I_D/(I_D+I_L)$. Figure 3.5, as an example, shows the EISF for $BaZr_{0.50}Sc_{0.50}O_{2.75}$ together with jump-diffusion models over two and four sites, respectively, which represent proton transfers (jump from one to another neighbouring oxygen atom) or rotational diffusion of the proton around one oxygen atom, accordingly [76, 77, 100, 101].

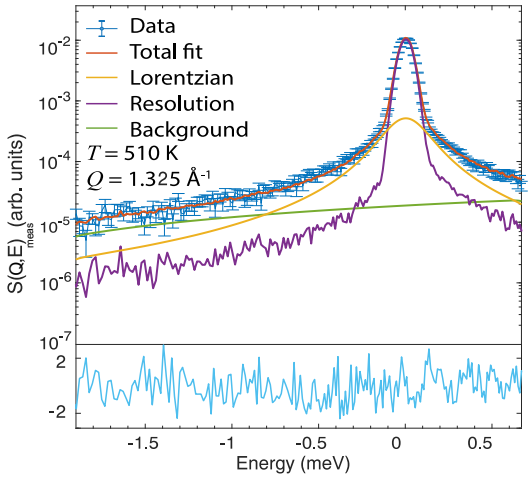

Figure 3.4: Examples of fitting results with one Lorentzian function to describe the quasielastic component on hydrated $BaZr_{0.50}Sc_{0.50}O_{2.75}$ measured on the IN6 instrument at Institut Laue-Langevin (Paper I).

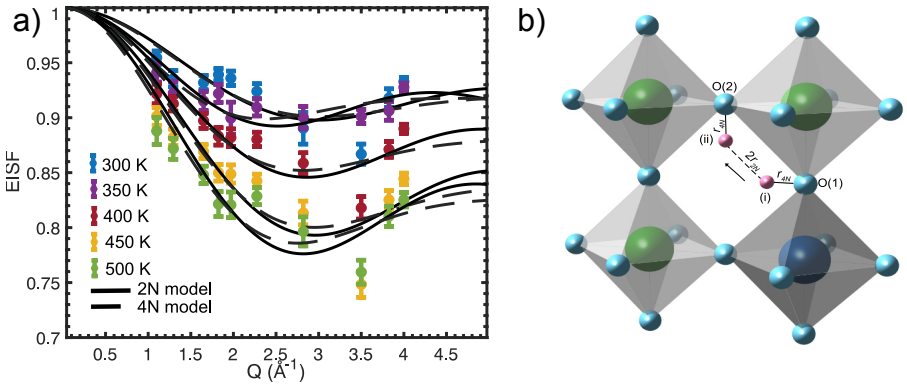

Figure 3.5: Extracted EISF for different temperatures of $BaZr_{0.50}Sc_{0.50}O_{2.75}$ as measured on the TOFTOF instrument at FRM II a). The data are compared to jump diffusion models over two (2N) and four (4N) sites. Schematic drawing of the perovskite structure along with the variables representing half of the jump distance (r_{2N}) and the rotations of the O–H band (r_{4N}) b). Note that the Zr atoms are green, whereas the Sc atom is blue, the oxygen atoms are turquoise and the protons are pink.

The jump diffusion models regarding jumps between two sites (2N) and jumps between 4 sites (4N) were fitted as per the following equations:

$$\mathrm{EISF}_{2N} = c + (1-c)\frac{1}{2}\left(1 + \frac{\sin(Q2r_{2N})}{Q2r_{2N}}\right) \tag{3.6}$$

$$\mathrm{EISF}_{4N} = c + (1-c)\frac{1}{4}\left(1 + \frac{2\sin(\sqrt{2}Qr_{4N})}{\sqrt{2}Qr_{4N}} + \frac{\sin(2Qr_{4N})}{2Qr_{4N}}\right) \tag{3.7}$$

where c can be interpreted here as extra elastic scattering due to "immobile" protons, i.e., protons that move too slowly to give QENS. In our QENS experiments on $BaZrO_3$ and $Ba_2In_2O_5$ powders, c was found to decrease with increasing temperature, which can be interpreted as a larger fraction of protons entering the time window of the instrument as their mobility increases with T, r_{2N} is half of the jump distance between neighbouring oxygen atoms and r_{4N} is the length corresponding to the O–H bond.

3.2 Infrared spectroscopy

IR spectroscopy is based on excitation of vibrational motions of atoms by electromagnetic radiation in the IR range and gives information about the specific vibrational frequencies and bond strengths present in the material undergoing a study. Explained with simple words, IR spectroscopy concerns balls (atoms) connected with springs (bonds), and the vibrations as a function of both the masses of the balls and the strength of the springs. Accordingly, the larger the mass of the atoms, the lower the frequency, and the stronger the bond, the higher the frequency. Essentially, this points towards that IR spectroscopy is in fact connected to the vibrations of corresponding frequencies with certain modes associated to a certain bond type [102]. For a certain material to have an IR spectral fingerprint, it must fulfil a selection rule which states that the dipole moment of the atoms consisting it, must change during vibration. Hence not all vibrations are IR active. For instance,

for homonuclear diatomics like O_2 or N_2 stretch modes are not IR active, whereas stretch modes of heteroatomic diatomics such as CO, HF, and OH are IR active [102]. As the primary concern of this study is the O–H stretch mode, further in this section we will discuss the O–H stretch mode characteristics in hydrated $BaZr_{1-x}Sc_xO_{3-x/2}$ (x = 0.10–0.65) powders and films, as well as hydrated $Ba_2In_{1.85}M_{0.15}O_5$ powders with M = In, Ga, Sc and Y.

When analysing IR spectroscopic data, vibrational modes are often assigned based on the presence of specific bonds which have a specific IR fingerprint. Some of the strongest (and shortest) bonds are formed with hydrogen and elements from the second row of the periodic table, such as oxygen. Hydrogen bonding is crucial in identification of structures of inorganic materials [102]. The O–H stretch modes are wildly affected by hydrogen bonds. For instance, sharp intense bands for free or isolated O–H groups are observed in the range of 3590–3690 cm^{-1}, however, in presence of hydrogen bonding, the O–H stretch band typically shifts to lower frequency.

3.3 Thermogravimetric analysis

TGA is a method that monitors mass changes as a function of temperature. TGA is, therefore, especially convenient for observing various chemical phenomena including, but not limited to, oxidation, desorption, vaporisation, dehydration, and solid-state reactions, which is why its application in material science as a characterisation tool is very diverse [103]. In this work, TGA has been used primarily for determining the hydration degree in hydrated powder samples of $BaZr_{1-x}Sc_xO_{3-x/2}$ (x = 0.10 and 0.50) and $Ba_2In_{1.85}M_{0.15}O_5$ (M = In, Ga, Sc and Y). These materials possess distinctive thermograms which are characterised with a broad slope typically in the interval between 300 °C and 500 °C upon increasing temperature, manifesting a gradual dehydration of the materials, followed by a final plateau as the TG curve for $Ba_2In_{1.85}Ga_{0.15}O_6H_2$ in Figure 3.6. However, for some proton conducting oxides the curves do not reach such a plateau even at temperatures beyond 900 °C. The reason for this behaviour is not fully clear, but may be associated with a release of strongly physisorbed water molecules and/or bulk protons, as seen in other studies on similar materials [104–106].

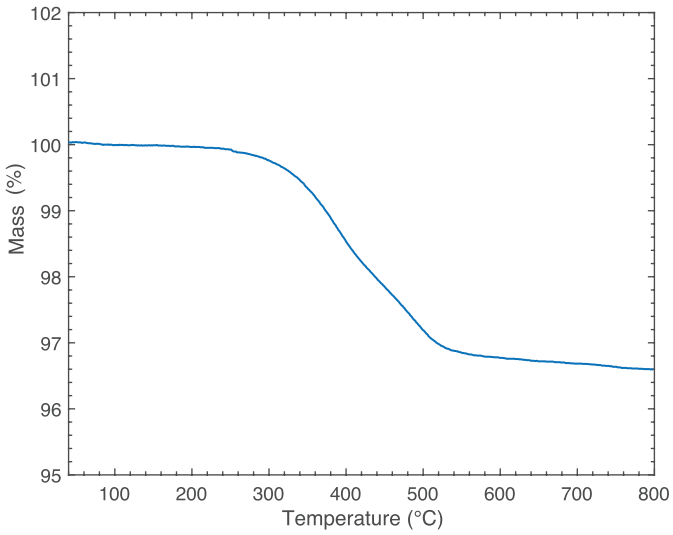

Figure 3.6: TG curve for a hydrated powder sample of $Ba_2In_{1.85}Ga_{0.15}O_6H_2$.

3.4 Nuclear Reaction Analysis

NRA is a convenient method for hydrogen depth profiling in film samples. In this thesis, $BaZr_{1-x}Sc_xO_{3-x/2}$ (x = 0.45, 0.54, and 0.64) films were subjected to NRA measurements. The fundamental principle behind NRA is that the film under investigation is exposed to accelerated and energy-monochromatized ^{15}N ions with energies in the range of E_{NRA} = 6.36-7 MeV which upon contact with hydrogen (protons) in the film undergo the following reaction:

$$^{15}N + {}^{1}H \rightarrow {}^{16}O \rightarrow {}^{12}C + \alpha + \gamma. \tag{3.8}$$

At the resonance energy E_R = 6.385 MeV, excited ^{16}O nucleus is formed as an intermediate compound, which then undergoes α-decay into the first nuclear excited state of ^{12}C, followed by release of γ-radiation with energy equal to 4.4389 MeV. The intensity of the γ-radiation signal is measured by a γ-detector and the intensity is related to the hydrogen density.

It is important to point out that ^{15}N ions with incident energy E_i equal to the resonant energy can only induce a nuclear reaction with the hydrogen atoms on the surface [107]. However, in the case of higher E_i, the ^{15}N ions penetrate further into the film sample, and they lose energy due to electronic stopping amid traveling through the film, $\Delta E_{NRA} = E_{NRA} - E_R$. Essentially, the energy loss ΔE_{NRA} is proportional to a certain depth, equivalent to the trajectory length of the penetrated ions, z, which is equal to zero at the surface [107], and can be calculated as $z = \Delta E_{NRA}/S$, where S is the stopping power which, in our case, is related to the total film thickness d and the energy E_d for which ions with energies larger than E_d can penetrate through the whole film without interaction with hydrogen, or, $S = (E_d - E_R)/d$. A schematic drawing of the fundamental process of NRA measurements on film samples is shown in Figure 3.7.

In our study, the energy resolution of the ^{15}N beam was taken to be around 13 keV, which corresponds to a depth resolution of the film of 50 Å, as previously determined by NRA measurements on a $BaZr_{0.53}In_{0.47}O_{2.765}$ 500 nm thick film [108]. The obtained results from the NRA measurements provide information of the total hydrogen content and hydration degree of the film samples which will be elaborated on further in this thesis.

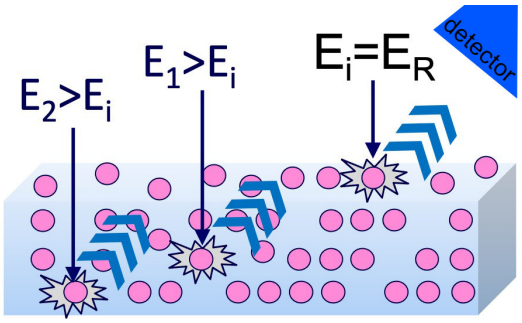

Figure 3.7: Schematic drawing of the basic principle of NRA for detection of the hydrogen as a function of distribution depth. Here, E_i represents the incident energy of the ^{15}N ions, and E_R the resonance energy equal to 6.385 MeV.

CHAPTER 4

Instruments

> Every brilliant experiment, like every great work of art, starts with an act of imagination.
>
> *Jonah Lehrer*

4.1 Instruments for quasielastic neutron scattering

There are a number of different types of instruments for performing QENS measurements. In this thesis, neutron time-of-flight (TOF) and backscattering instruments were used. The most notable difference between the two types of instruments lays in the determination of the neutron energy transfer $\Delta E = E_i - E_f$, where E_i is the incident neutron energy and E_f is the final neutron energy. The TOF instruments used in this thesis rely on a, so called, direct geometry, which means that we have neutrons with fixed E_i which hit the sample and scatter to the detector. The final neutron energy is then determined by measuring the time the neutron needs to reach the well defined distance between the sample and the detector. Backscattering scattering instruments, on the other hand, have an indirect geometry which means that the final neutron energy is selected by Bragg reflection from an analyzer crystal (in our case a Si crystal), whereas the incident neutron energy is allowed to vary. While traditionally backscattering instruments have a Doppler-moving monochromator for changing the incident energy, the instrument used in this thesis is a spallation source-based, which means that the built-in neutron pulsed structure is used as an E_i wavelength. The neutrons hit the sample and backscatter from an analyser and scatter on the detector positioned at Bragg angle 2Θ close to 180° to achieve highest energy resolution[1] (thus fixing the final neutron energy) before finally reaching the detector.

The main difference when using these two techniques lies in the energy resolution, which due to the Bragg angle close to 90°, is much higher (μeV range) for the backscattering technique.

4.1.1 The neutron TOF instruments IN6 and TOFTOF

As part of this thesis, two TOF instruments, IN6 and TOFTOF were used for analysis of the localised proton motion in Sc doped $BaZrO_3$. IN6 is a TOF instrument at ILL, in Grenoble, France.

[1] In terms of differentiated Bragg's law, $\delta E_f = 2E_f(\frac{\delta d}{d} + \cot\Theta\delta\Theta)$, where Θ is the Bragg angle and $\frac{\delta d}{d}$ is the spread of the analyzer's lattice constants, the $\cot\Theta\delta\Theta$ is minimized as Θ approaches 90°. This implies that the only the analyzer will influence the convergence of the beam [109].

Monochromatization of the polychromatic neutron beam is achieved by graphite monochromators which is then chopped by a Fermi chopper. The scattered neutrons are then detected by 337 He detectors covering scattering angles between 10°and 115° [99, 110]. In our experiments, the spectrometer operated with 5.1 Å incident wavelength neutrons, yielding an energy resolution of 0.07 meV at full width at half maximum (FWHM) at the elastic line, and an accessible Q-range of 0.21–2.08 Å^{-1}. Schematic drawing of IN6's configuration is shown in Figure 4.1 (a).

TOFTOF is an instrument at the FRM II Neutron Source in Garching, Germany. The beam is monochromatized and pulsed by seven fast rotating disc choppers and is then focused onto the sample by a converging supermirror. The scattered neutrons are detected by 1000 He detectors covering scattering angles between 7°and 140° [111]. For our experiments, TOFTOF operated with 2.5 Å incident wavelength neutrons, yielding an energy resolution of 0.45 meV at FWHM at the elastic line, and an accessible Q-range of 0.35–4.72 Å^{-1}. Schematic drawing of TOFTOF's configuration is shown in Figure 4.1 (b).

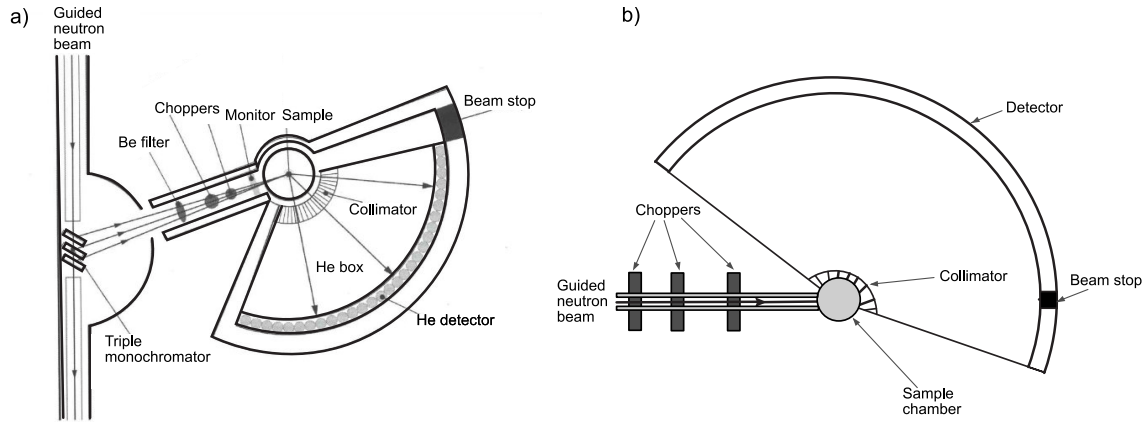

Figure 4.1: Schematic drawing of a) the IN6 and b) the TOFTOF instrument. The figure is taken from [111–113].

4.1.2 The neutron backscattering instrument BASIS

As part of this thesis, the instrument BASIS was used for analysis of the localised proton motion in hydrated $Ba_2In_{1.85}M_{0.15}O_5$ with M = In, Ga, Sc and Y. BASIS is a backscattering, crystal-analyzer spectrometer situated at the Spallation Neutron Source at Oak Ridge Laboratory in the US. It is characterised with an energy resolution up to 3.5 μeV for Si(111) analyzer (or 15μeV for Si(311) analyzer), and accessible timescales from 2 ps to 0.1 ns. It can likewise access an extended Q range up to 3.8 Å^{-1} with Si(311) analyser, compared with the upper 2.0 Å^{-1} limit for Si(111) analyser. For our experiments, the spectrometer operated with Si(111) analyser, yielding an energy resolution of 3.5 μeV at FWHM at the elastic line, and an accessible Q-range of 0.2–2.0 Å^{-1}. Schematic drawing of a traditional backscattering instrument configuration is shown in Figure 4.2. A comparison of some important characteristics of the instruments used in this thesis are presented in Table 4.1.

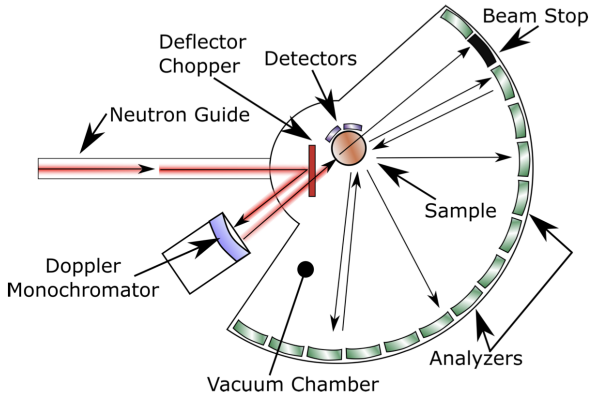

Figure 4.2: Schematic drawing of a traditional backscattering instrument. Note that BASIS does not have a Doppler monochromator. The figure is taken from ref [114].

Table 4.1: Some characteristics of the IN6, TOFTOF and BASIS instruments used for QENS measurements in this thesis.

	IN6, ILL	**TOFTOF, FRMII**	**BASIS, SNS**
Neutron source: **Neutron flux:**	Reactor source 1.5 10^{15} neutrons/s cm^2	Reactor source 10^{14} neutrons/s cm^2	Spaliation source 60 pulses/second
Instrument type:	Time-of-flight (direct geometry) E_i is fixed by graphite crystal	Time-of-flight (direct geometry) E_i is fixed by choppers	Backscattering (indirect geometry) E_f is fixed by analyzer
Wavelength:	5.1 Å	2.5 Å	6.267 Å
Probed timescale:	Picosecond (100 ps)	Picosecod to ns (up to 50 ns)	Picosecond to nanosecond
Probed Q range:	0.21–2.08 Å^{-1}	0.35–4.72 Å^{-1}	0.2–2.0 Å^{-1}

4.2 The IR spectrometer Thermo Scientific Nicolet Nexus

In the past, IR spectrometers were equipped with various prisms, thermal detectors and diffraction gratings connected to a recorder. Nowadays, almost every IR spectrometer uses interferometers and Fourier transform data processors, known as Fourier transform IR spectrometers (FTIRs) [102, 115].

The basic working principle of a FTIR spectrometer is as follows: a IR light source (usually a ceramic material that is heated to high temperatures which results in IR radiation) is defined by an aperute and is partially transmitted and partially reflected to a moving mirror by a beam splitter. The moving mirror creates an interferogram *quod est* Fourier transformed into a spectrum [116]. FTIR spectrometers are single-beam instruments so both background and sample spectra need to be recorded as separate measurements. The final spectrum is then obtained by the ratio of the two spectra. The FTIR spectrometer used for this thesis is a Thermo Scientific Nicolet Nexus instrument (Figure 4.4) and the two sampling techniques used in this thesis are the transmittance mode for the film samples and diffuse reflectance mode for the powder samples. The first is based on the principle that the incident light passes through the whole sample, whereas the second is based on the diffuse reflection of the incident light by the powder's surface reflection in all directions. For the film samples, a background spectrum was taken on the Al_2O_3 substrate which is almost transparent in the IR range, whereas for the powder samples, the diffuce reflectance background accessory (mimicking perfect diffuse scattering) was used. It is important to point out that for the films, due to the large thickness of the substrate there was a strong interference which was smoothed using the Savitzky-Golay algorithm in the Thermo Scientific OMNIC FTIR software.

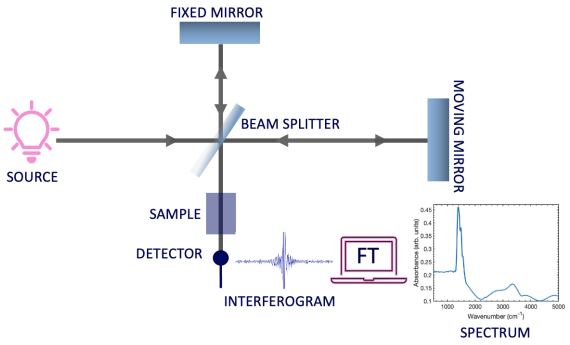

Figure 4.3: Schematic drawing of a FTIR spectrometer configuration. The light from the IR source is impinged on a beam splitter which is then partially transmitted and reflected to the fixed and moving mirrors. Due to the moving mirror's alternation, an interferogram is generated. The interferogram is then converted to a spectrum by a Fourier transformation.

4.3 The TGA instrument STA 409 PC Luxx thermal and calorimetric analyser

The instrument used for this work is the STA 409 PC Luxx thermal and calorimetric analyser which operates from room temperature into the high temperature range of 2000 °C. The measurements were performed using a thermobalance which includes an electronic balance (with microgram precision), a temperature–programmable furnace and computer–driven controller which enables simultaneous heating and weighing of a sample. Figure 4.4 shows a schematic drawing of the components consisting the instrument. The working principle is as follows; initially, the sample is placed and weighed in a crucible (for our experiments an alumina crucible was used due to its resistance to high temperature and non-reactivity with the $BaZrO_3$ and $Ba_2In_2O_5$ powders). Then, the sample is heated to higher temperatures with a constant heating rate, or in our case between 800–1000 °C with 5–10 °C/min. The sample is situated within an enclosed system ensuring a gaseous atmosphere of the measurement. In our case the instrument was connected to nitrogen gas to prevent possible oxidation.

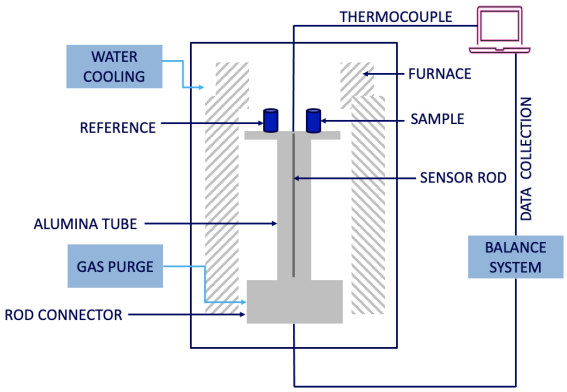

Figure 4.4: Schematic drawing of the STA 409 PC Luxx thermal and calorimetric analyser's configuration. The sample is put on the balance within the furnace and mass change is detected as a function of temperature.

CHAPTER 5

Overview of Findings

I never see what has been done; I only see what remains to be done.

Marie Curie

5.1 Paper I

This paper reports on the nature of localized proton dynamics in hydrated powder samples of Sc doped $BaZrO_3$ with two significantly different Sc dopant concentrations, $BaZr_{0.90}Sc_{0.10}O_{2.95}$ (10Sc/BZO) and $BaZr_{0.50}Sc_{0.50}O_{2.75}$ (50Sc/BZO) using QENS. The aim of the study is to see how the Sc doping concentration influences the localised proton diffusion. The two samples were first measured on IN6, followed by another measurement on TOFTOF. The complementary in the two measurements for this study lays in the fact that they probe different timescales which give information about different types of motions present in the materials, or in our case slightly faster motions up in the ps for TOFTOF. Likewise, the measurement on TOFTOF allowed to get extended Q range up to 4.72 $Å^{-1}$ which gives physically more reasonable results due to the increased statistics (more Q points), compared to the 2.08 $Å^{-1}$ Q range accessed with IN6. The extended Q range was used to also try to get more precise results regarding the preferred EISF model as the bifurcation point that separates the 2N and 4N models occurs at Q points higher than the one obtained from IN6 [117]. Figure 5.1 shows, as an example, $S(Q,E)_{\text{meas}}$ for both materials and as measured on both instruments for highest measured temperatures (T = 510 K for IN6 and T = 485 K for TOFTOF) and high Q (Q= 1.3 $Å^{-1}$ for IN6 and Q= 4.0 $Å^{-1}$ for TOFTOF).

From the IN6 measurements, analysis of the FWHM (Γ) of the Lorentzian function showed that it is (within error) Q-independent, for each sample and measuring temperature, indicating localised dynamics. The FWHMs were found to be between 0.2 and 0.5 meV, depending on Sc dopant concentration and temperature for the IN6 data, which results in relaxation timescales in the range of 4 and 8 ps and activation energies between 25 and 40 meV. The values are in agreement with previous studies on the same materials where the activation energy was in the interval in the range of 10 meV and 30 meV [118]. As for the geometry of the localised motion, only the EISF-extracted jump distances and rotational motions from TOFTOF were used.

From the TOFTOF measurements, analysis of the FWHM (Γ) of the Lorentzian function showed that it is (within error) Q-independent, for each sample and measuring temperature, indicating localised dynamics yet again. The timescale of the proton dynamics was then found to be in the range of 1.8 and 2.5 ps for 10Sc/BZO and 1.5 and 1.8 ps for 50Sc/BZO, whereas the activation

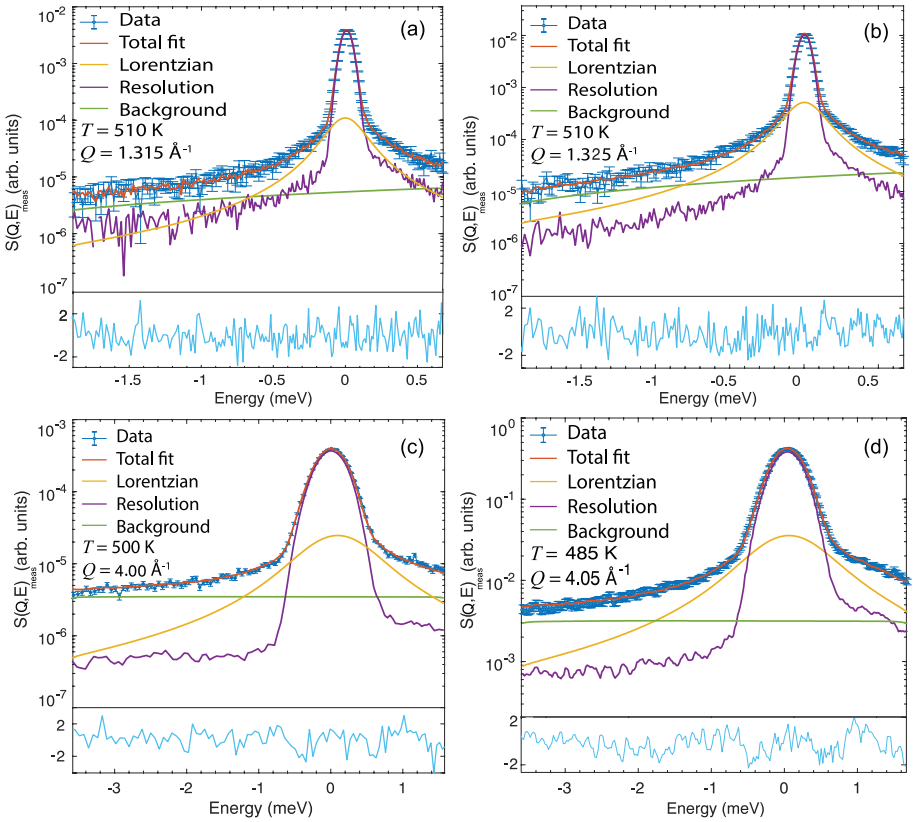

Figure 5.1: $S(Q,E)_{\text{meas}}$ together with fits of (a) 10Sc/BZO and (b) 50Sc/BZO at $T = 510$ K and $Q = 1.315$ Å^{-1} and $Q = 1.325$ Å^{-1}, respectively, as measured on IN6, and (c) 10Sc/BZO and (d) 50Sc/BZO, as measured on TOFTOF at $T = 485$ K and $Q = 4.0$ Å^{-1}.

energies were found to be between 8 and 25 meV. The EISF showed that the proton transfers were in the interval between 0.75 and 0.79 Å and 0.94 and 1.03 Å for –OH rotational motions for 10Sc/BZO, and 0.76 and 0.82 Å for proton transfer and 0.95 and 1.06 Å for –OH rotational motions for 50Sc/BZO. From the fit itself it was not possible to clearly distinguish the preferred motion (transfer or rotational), as seen in Figure 5.2. However, the low values of the activation energy[1] in combination with *ab initio* calculations showed that the rotational motion has been predominant. This is further supported by the low activation energies below 100 meV attributed to the reorientation motion [119].

The slightly faster timescales, lower activation energy and a slightly larger fraction of mobile protons freed at higher temperatures observed for 50Sc/BZO could be ascribed to the increase in the proportion of asymmetric units Sc–O–Zr. As a consequence, a relatively higher population of proton transfers with shorter jump distances are expected in 50/ScBZO, compared to 10Sc/BZO. Since the activation energy for the proton transfer is related to the jump length, a shorter proton transfer jump length, averaged over all proton transfer contributing in the QENS signal, as well as a predominant –OH rotation motion could possibly explain the lower activation energies found in 50Sc/BZO than in 10Sc/BZO.

It can be concluded that the QENS signal of 50Sc/BZO can be ascribed to contributions from different proton transfer and –OH rotation motions, over a large range of timescales, with no sig-

[1]Proton transfer requires breaking of the O–H bond which is a more energetically costly process.

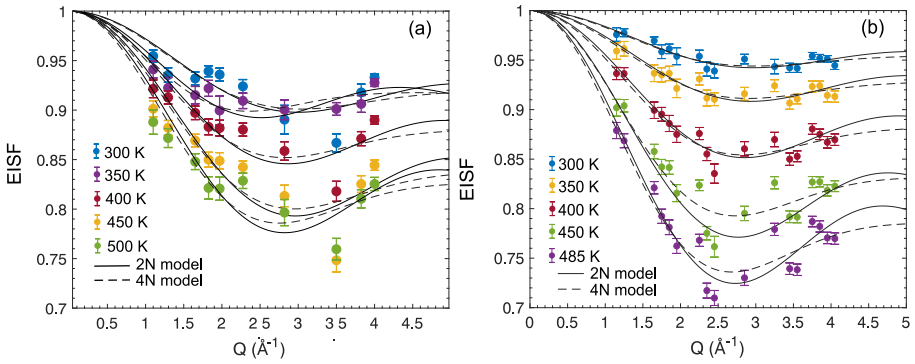

Figure 5.2: EISFs for (a) 10Sc/BZO and (b) 50Sc/BZO, as derived from the TOFTOF data. The lines are fits to the jump-diffusion model over two (2N) and four (4N) sites.

nificant differences in activation energies or in the geometrical representation of the dynamics, as compared to 10Sc/BZO. It is also shown that access to momentum transfers of at least 4 Å^{-1} in the QENS data is a necessary for extracting physically meaningful jump distances for the proton transfer and –OH rotational process.

5.2 Paper II

This paper reports on the nature of localized proton dynamics in hydrated powder samples of undoped and acceptor doped $Ba_2In_2O_5$, i.e., $Ba_2In_{1.85}M_{0.15}O_5$ with M = Ga, Sc and Y using QENS. The aim of the study is to see if the introduction of different dopants in the $Ba_2In_2O_5$ structure changes the localised proton diffusion. The paper is a continuance of a recent QENS study which revealed that there are three localised processes present in hydrated $Ba_2In_2O_5$ [90]. In more detail, it showed two types of proton sites H(1) and H(2) associated with proton reorientations with low activation energy E_a = 19.3 meV in the range of 2.8–4.6 ps, and proton transfers of H(2) protons between neighbouring oxygens with E_a = 13.4 meV, in the range of 0.4–0.5 ps, respectively. It was also pointed out that a mixture of proton transfers and reorientations with E_a = 35 meV, in the range of 45–77 ps is attributed to a third proton site H(3). The hydrated powder samples of $Ba_2In_{1.85}M_{0.15}O_5$ with M = In, Ga, Sc and Y were measured on BASIS. The spectrometer operated with Si(111) analyser, yielding to an accessible Q-range of 0.2–2.0 Å^{-1}.

Figure 5.3 (a) shows $S(Q,E)_{\text{meas}}$ for $Ba_2In_2O_5$ for highest measured temperature T = 600 K and Q = 1.5 Å^{-1} along with a fit composed of one Lorentzian function. Analysis of the FWHM of the Lorentzian function showed that it is Q-independent, indicating localised dynamics in the range of 7–10 ps and activation energy E_a = 35 meV. Analysis of the O–H stretch region of the IR spectra (2000–3500 cm^{-1}), as seen in Figure 5.4, revealed a broad band peaking at around 3400 cm^{-1} shifted to higher frequencies attributed to a presence of a larger fraction of protons on the H(1) site.

Figure 5.3 (b) shows $S(Q,E)_{\text{meas}}$ for $Ba_2In_{1.85}Ga_{0.15}O_5$ for highest measured temperature T = 490 K and Q = 1.5 Å^{-1} along with a fit composed of two Lorentzian functions. Analysis of the FWHM of the first Lorentzian function confirmed localised dynamics in the range of 7–20 ps and activation energy E_a = 179 meV. Analysis of the FWHM of the second Lorentzian function revealed a second localised motion of 36 ps emerging for temperatures above T = 490 K. Analysis of the O–H stretch region of the IR spectra (2000–3500 cm^{-1}), as seen in Figure 5.4, revealed a broad band peaking around 3450 cm^{-1} shifted to lower frequencies, and additional band at around

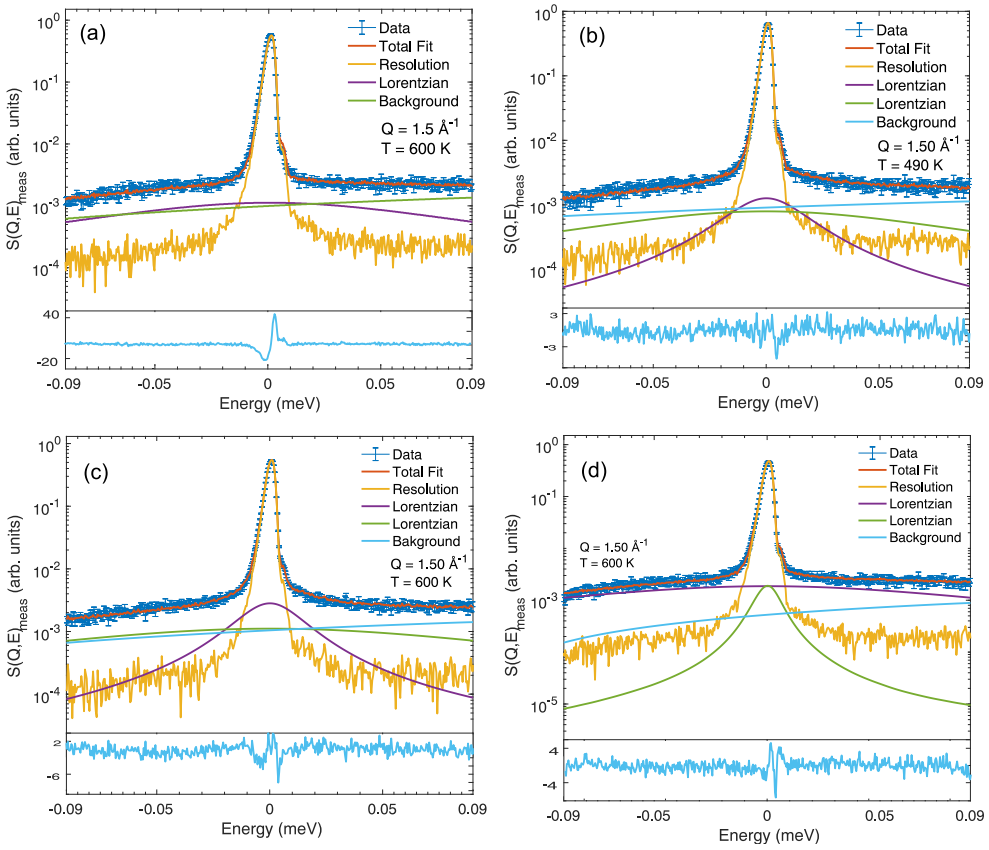

Figure 5.3: $S(Q,E)_{\text{meas}}$ of (a) $Ba_2In_2O_5$, (b) $Ba_2In_{1.85}Ga_{0.15}O_5$ at $T = 490$ K, (c) $Ba_2In_{1.85}Y_{0.15}O_5$ at $T = 600$ K and (b) $Ba_2In_{1.85}Sc_{0.15}O_5$ at $T = 600$ K for $Q = 1.50$ Å^{-1} together with fits.

2000 cm^{-1} indicating a presence of a larger fraction of protons on the H(2) site.

Figure 5.3 (c) shows $S(Q,E)_{\text{meas}}$ for $Ba_2In_{1.85}Y_{0.15}O_5$ for highest measured temperature $T = 600$ K and $Q = 1.5$ Å^{-1} along with a fit composed of two Lorentzian functions. Analysis of the FWHM of the first Lorentzian function confirmed localised dynamics in the range of 6–20 ps and activation energy $E_a = 101$ meV. Analysis of the FWHM of the second Lorentzian function revealed a second localised motion in the range of 44–50 ps emerging for temperatures above $T = 490$ K. Analysis of the O–H stretch region of the IR spectra (2000–3500 cm^{-1}), as seen in Figure 5.4, revealed a broad band peaking around 3450 cm^{-1} and shifted to lower frequencies, as well as an additional band at around 2000 cm^{-1} attributed to a presence of a larger fraction of protons on the H(2) site. Figure 5.3 (d) shows $S(Q,E)_{\text{meas}}$ for $Ba_2In_{1.85}Sc_{0.15}O_5$ for highest measured temperature $T = 600$ K and $Q = 1.5$ Å^{-1} along with a fit composed of two Lorentzian functions. Analysis of the FWHM of the first Lorentzian function confirmed localised dynamics in the range of 6–8 ps and activation energy $E_a = 32$ meV. Analysis of the FWHM of the second Lorentzian function revealed a second localised motion in the range of 127 ps emerging for temperatures above $T = 600$ K. Analysis of the O–H stretch region of the IR spectra (2000–3500 cm^{-1}), as seen in Figure 5.4, revealed a broad band peaking at around 3500 cm^{-1} and shifted to higher frequencies which has been assigned to a presence of a larger fraction of protons on the H(1) site.

Because of the QENS signal's high uncertainty, the proton motion was ascribed as a mixture of proton transfers with various jump lengths and –OH rotation motions, rather than to a specific

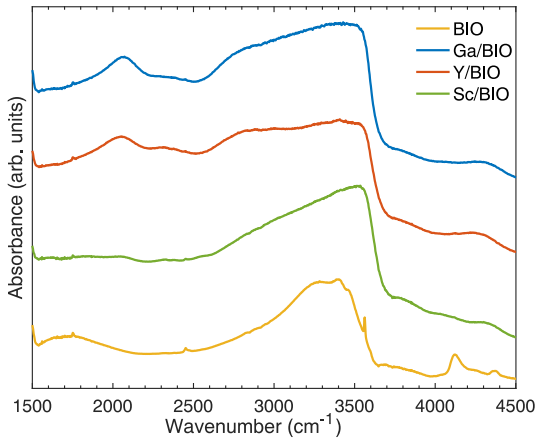

Figure 5.4: IR spectra for the hydrated powder samples of $Ba_2In_{1.85}M_{0.15}O_5$ with M = In, Ga, Sc and Y. Note that the broadness of the O-H stretch band is due to a range of different local proton environments in the samples.

proton transfer or –OH rotation motion. Accordingly, the obtained activation energies and residence times would then represent an average of contributions from both proton transfers and rotation motions. The assigned bands at ca. 2000–2100 cm^{-1} and 2800–3000 cm^{-1} to protons on the H(2) site are more pronounced for the Ga/BIO and Y/BIO systems, indicating that the dominating localized motion is the proton transfer [90, 120]. On the other hand, the other systems with more pronounced band peaking at ca. 3300 cm^{-1} could be ascribed to a larger fraction of protons populating the H(1) site and a dominating proton transfer motion. Furthermore, the slower motion obtained for the samples doped with Sc, Ga, and Y, at temperatures higher than 450 K is likely related to a site H(3), where the hydrogen is covalently bonded to oxygen in the pseudo-cubic layer and hydrogen bonded to oxygen connecting the two layers [90]. The different proton configuration depending on the dopant atom may be due to the different size of the ionic radii of the dopant atoms, as more pronounced H(2) sites are observed for the systems with dopant that vary significantly in size in respect to In, i.e. Ga (much smaller) and Y (much larger).

To conclude, doping the $Ba_2In_2O_5$ structure has a significant effect on the local structure and dynamics of protons. In particular, doping with M = Ga or Y, both with significantly different radii than In, results in larger contribution of protons on the H(2) site, corresponding to a presence of predominant proton transfers, as opposed to doping with M = Sc or In where a larger contribution of protons on the H(1) site corresponding to a presence of predominant proton reorientation motion. It can also be concluded that doping the $Ba_2In_2O_5$ structure results in a presence of an additional slower motion which is attributed to a mixture of transfer and rotational motions.

5.3 Paper III

This paper reports on the nature of the local structure and coordination of protons and its dependency on the morphology on nanocrystalline $BaZr_{1-x}Sc_xO_{3-x/2}$ films with $x = 0.45, 0.54, 0.65$. The specific aim of the study was to investigate and compare the local structure, especially regarding the concentration and local coordination environments of the protons, between the microcrystalline

powder samples of similar doping concentration and nanocrystalline film samples, and their link to the proton concentration.

As can be seen in Figure 5.5, hydrogen concentration of the films for all concentrations was found to be below 33% (of 100% which corresponds to full hydration) with large concentration of protons, i.e., between 0.15–0.16 hydrogen atoms per unit cell, located in the surface pointing out of a proton rich layer present in the films, [108] as well as indicating that either the films were not fully hydrated or that there are less oxygen vacancies present in the system.

As can be seen in Figure 5.6, the spectra show considerable differences amongst the samples. For the powder samples, a large O-H stretching band between 2500 and 3700 cm^{-1} is dominating, and O-H stretching + wagging combination band at around 4350 cm^{-1} is visible; in general there is a trend of increasing band intensity with increasing doping concentration, which is in agreement with previous studies on the same and similar compositions [69, 76, 77, 121]. The broadness of the O-H stretch band is due to a range of different local proton environments in the samples, where the lower-frequency part (2500–3000 cm^{-1}) is assigned to protons in non-symmetrical environments, such as Zr–O–Sc, whereas the higher-frequency part (3000–3700 cm^{-1}) is assigned to protons in symmetrical environments, such as Zr–O–Zr and Sc–O–Sc [82]. It can be seen that the change in band profile with increasing Sc dopant level is a result of differences in the distribution of protons in various types of proton sites. On the other hand, the film samples are characterized by much weaker and narrow bands, which suggests that the proton site distribution is less homogenous in the films with a larger fraction of protons in symmetric, weakly hydrogen-bonding configurations.

Based on the findings, a threshold for formation of a preferred proton site for the film samples is possibly between $x = 0.45$ and $x = 0.54$. Because the average particle distribution is not significantly affected by the increase of Sc dopant concentration, the threshold has been likely associated with a change in the local structural details of the films. These structural disortions may be induced by tilts of the octahedral moieties due to the increased Sc dopant concentration and mechanical stress from the film's substrate. Therefore, above a certain threshold composition between $x = 0.45$ and $x = 0.54$, the local structural distortions probably reached a certain level to form a unique local proton configuration, featured by weak hydrogen-bonding interactions in the films.

It can be concluded that for the film samples there is possibly a preferred and highly symmetrical local proton environment, as well as an inhomogeneous distribution of protons with high concentration located on the near-surface region, which suggests that there may be a proton rich top layer. The presence of a near-surface proton rich layer was likewise recently reported on hydrated, epitaxial, thin ($\approx$ 50 nm) film samples of the similar material $BaZr_{0.53}In_{0.47}O_{2.77}$, [108] which suggests that this could be a generic feature of proton conducting perovskite films.

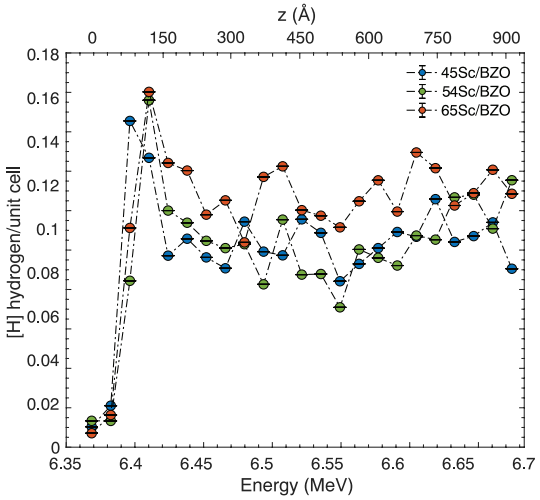

Figure 5.5: Hydrogen concentration of the hydrated film samples of $BaZr_{1-x}Sc_xO_{3-x/2}$ with $x = 0.45$, 0.54, and 0.65, as derived from NRA. The top axis shows the estimated penetration depth. The error bars were calculated as a standard deviation with 95% certainty and are within the data points. (Paper III).

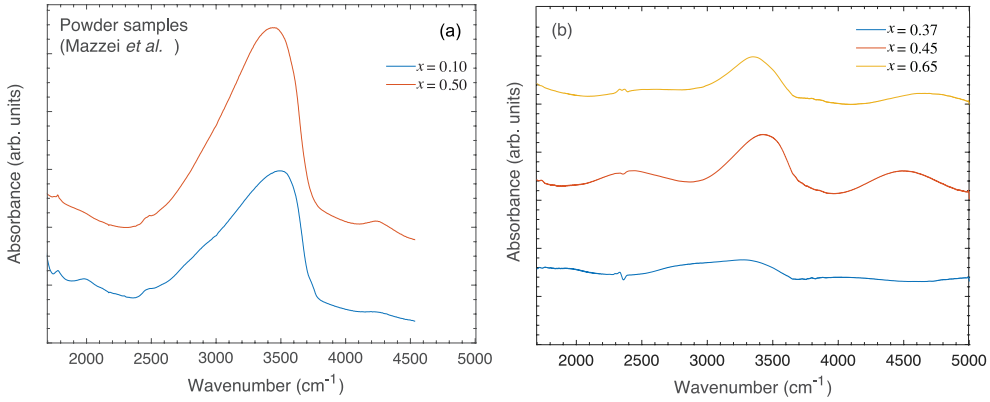

Figure 5.6: Comparison between the O–H region of the bulk powder samples from ref. [83] (a) and the film samples (b).

CHAPTER 6

Conclusions

> What is research but a blind date with knowledge?
>
> *Will Harvey*

The research results presented in this thesis have contributed to the field of proton conducting oxides as they provided a more thorough understanding of the localised proton motion and structure in proton conducting perovskite and perovskite-like structures. Essentially, the results dived more deeply in understanding the relationship of the dopant atom and dopant concentration with the localised preferred motion of the proton as well as the preferred site of the protons. This thesis has reported on investigations related to the structure and dynamics in some particularly important proton conducting perovskite materials relevant for several energy applications, such as fuel cells.

In more detail, the studies of powder samples of $BaZr_{1-x}Sc_xO_{3-x/2}$ (x = 0.10 and 0.50) confirmed localised proton dynamics ascribed as reorientation motions around one oxygen and transfer of protons from one to another neighbouring oxygen. The processes for both doping concentrations were shown to be in the range of 1–10 ps with activation energies between 8–40 meV. Likewise, it was found that these values depend insignificantly on the Sc dopant levels investigated in this study. The study of films of $BaZr_{1-x}Sc_xO_{3-x/2}$, (x = 0.45, 0.54, 0.65) pointed towards the presence of a wide range of local surroundings of the protons for x = 0.45, as opposed to the compositions with x = 0.54 and 0.65, which suggested a presence of relatively symmetric, weakly hydrogen-bonding, proton configurations. It was also shown that the films investigated here exhibit significantly different local structure than powder samples of similar compositions. The study on hydrated powders samples of brownmillerites $Ba_2In_{1.85}M_{0.15}O_5$ with M = In, Ga, Sc and Y showed the presence of localised proton transfer and –OH rotational motions of H(1) and H(2) protons on the picoseconds timescale, respectively, for temperatures above 400 K, independent on the dopant atom. For dopants with significantly different ionic radii compared to In, i.e., M = Ga and Y, it was found that a larger fraction of protons are present on the H(2) site, as opposed to M = Sc and In, where there is a larger fraction of protons on the H(1) site. It was likewise discovered that doping with with M = Ga, Sc and Y give rise to an additional proton site H(3) at temperatures above 450 K, which is a mixture of both proton transfer and reorientation motions.

A better understanding in the proton dynamics and how it varies with the structure and dopant atom and doping concentration is still needed for developing strategy for tuning current synthesis routes for obtaining materials with high proton conductivity that can be used in various electrochemical devices. And although the perovskites are indeed the most promising candidate, one still needs to question whether there are next generation materials pending to be discovered and if so *quo vadis*?

CHAPTER 7

Outlook: Quo Vadis?

> The important thing is to never stop questioning.
>
> *Albert Einstein*

7.1 Research related to perovskite proton conductors

With a view towards the future, this thesis has opened up several new questions well worth investigating. As one example, the results for Sc doped $BaZrO_3$ powder and film samples pointed towards a different structure between the two types of samples. This, in turn, suggests that further studies of the local structure of these films would be important. Raman scattering is a convenient technique for investigation of local structure and vibration properties of proton conducting oxides. However, Raman spectroscopy is inconvenient for investigations of film samples, as the weak Raman signal from the sample is overwhelmed by the background signal from the substrate; furthermore the penetration of the incident light is limited by its wavelength typically between 400–700 nm. In comparison, UV Raman spectroscopy which utilises an excitation energy in the ultraviolet region, is convenient for investigations of thin film samples as its penetration depth is reduced compared to conventional Raman scattering which minimizes the substrate signal while at the same time enhances the signal from the sample. Therefore, UV Raman spectra were measured on the $BaZr_{1-x}Sc_xO_{3-x/2}$ films with $x = 0.45$, 0.54, 0.65 by collaborators in Uppsala University. The measurements were recorded over the frequency range 200-2400 cm^{-1} in backscattering geometry. Excitation was performed using 355 nm (3.49 eV) and 405 nm (3.06 eV) wavelengths.

Figure 7.1 shows (preliminary) UV Raman spectra of $BaZr_{1-x}Sc_xO_{3-x/2}$ films with $x = 0.45$, 0.54, 0.65 films excited with 355 nm wavelength, from 200 cm^{-1} up to 1200 cm^{-1} and with 405 nm from 200–2400 cm^{-1}. Different excitation wavelengths were used to see differences in the excited vibrations. Because the films were fairly inhomogeneous, additional measurements at different parts of the samples were performed, denoted spot 2 or spot 3 in Figure 7.1. One can observe five different peaks present for all samples at around 380 cm^{-1}, 420 cm^{-1}, 450 cm^{-1}, 575 cm^{-1}, and 750 cm^{-1}. The lowest doped system with $x = 0.45$ shows significantly lower peak intensity than the other two compositions. Clear increase in intensity is observed between the $x = 0.54$ and the $x = 0.65$ spectra. Figure 7.1 shows the UV Raman spectra excited at 405 nm. A total of 11 different peaks are observed. A small peak at around 375 cm^{-1}, followed by a strong sharp peak at 415 cm^{-1} and its shoulder peak at around 430 cm^{-1}, a small peak at 450 cm^{-1}, followed by a peak at 575 cm^{-1}. Broad small peaks are likewise observed at 640cm^{-1} and 750cm^{-1}. Rather broader peaks are

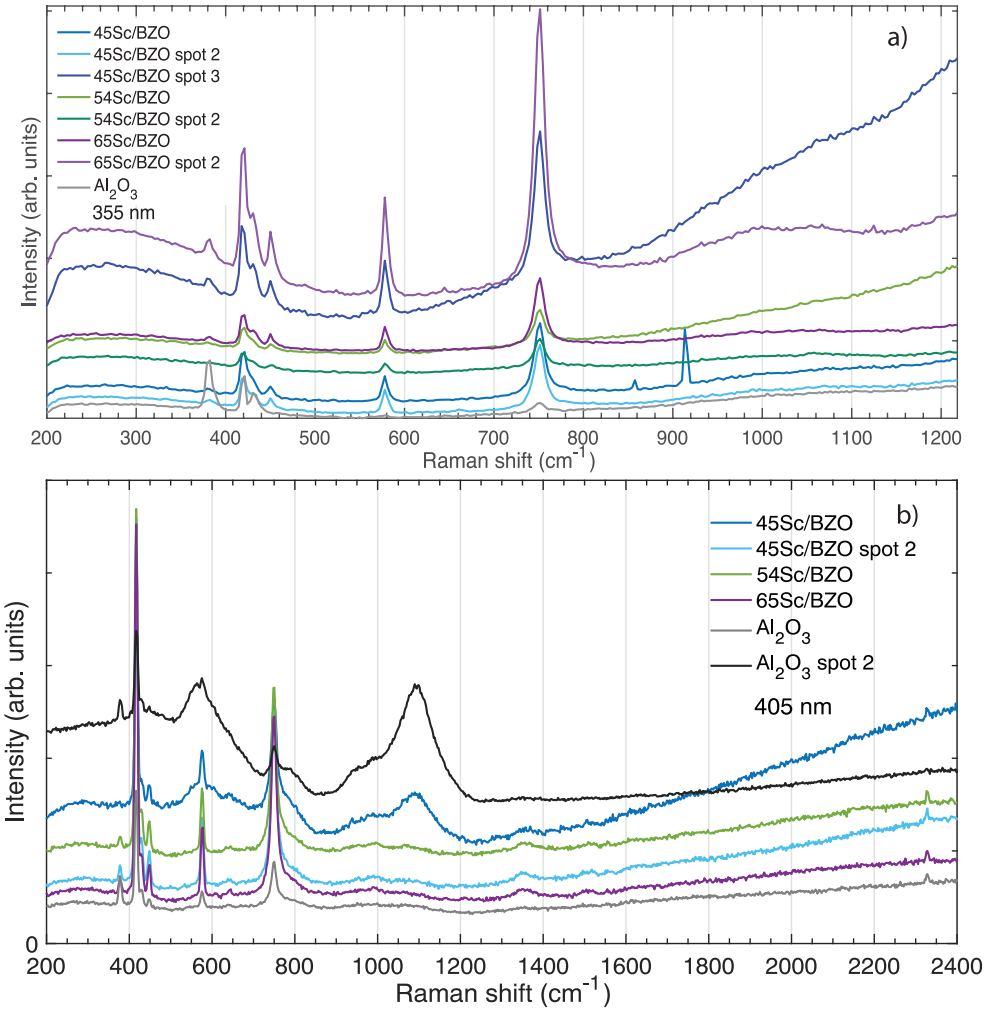

Figure 7.1: UV Raman spectra as recorded for the thin film samples for excitation at 355 nm a) and 405 nm b). The spectra are vertically shifted for clarity.

observed at around 990 cm^{-1}, 1345 cm^{-1} and 1505 cm^{-1}. Small peak is likewise observed at around 2330 cm^{-1}. The peaks at 575 cm^{-1} and 750 cm^{-1} are increasing with intensity with increasing the doping concentration. One can also see that the influence of doping on the peak intensity is strong.

Previous results on bulk materials with the same or similar composition, suggest that the bands positioned in the interval between 400 and 800 cm^{-1} are related to different oxygen motions suggesting displacement of the cations and the oxygens from their initial symmetric sites [122, 123].

The analysis of the data is ongoing and aims to contribute to a better understanding of the local structure of the (thin) film samples of Sc doped $BaZrO_3$.

Also, based on the results from the study of Sc doped $BaZrO_3$ films, new $BaZr_{1-x}Sc_xO_{3-x/2}$ films with $x = 0.15, 0.45, 0.65$ based on PLD technique will be prepared in order to see if there is any difference in terms of structure of the films when using another deposition technique. The newly developed films will be investigated with vibrational spectroscopy techniques (IR, and UV Raman). The deposition will be performed by collaborators from Paul Scherrer Institute.

7.2 Research related to perovskite oxyhydrides

Building further on my research pertaining to investigations of structure and dynamics in proton conducting perovskites, I have recently started some research on perovskite type oxyhydrides. Similarly to proton conducting oxides, these materials contain hydrogen, but now the hydrogen is in the form of hydride ions (H^-) rather than protons (H^+).

Oxyhydrides as a class of mixed anion compounds has attracted significant interest due to their possible contribution in energy devices, catalysis or electronics [124]. Scientists aim to develop novice synthesis methods beyond the classical solid state route, including but not limited to topochemical synthesis, mechanochemical synthesis reduction-based synthesis and etc [124].

My main focus so far has been to design new synthesis methods and also design new classes of oxyhydrides. Accordingly, several synthesis methods based on topochemical reaction (hydrogen gas reduction and metal hydride reduction) and mechanochemical reactions have been tried.

For the topochemical synthesis using metal hydrides, performed at Stockholm University, the aim was to use reduction agents beyond the traditionally used CaH_2, or in my case LiH for the synthesis of $BaTiO_3$ oxyhydride powder samples. Synthesis method based on mechanochemical synthesis was likewise tested at Stockholm University. Mechanochemical synthesis is especially useful for the industry as it shortens the synthesis time from few days to few hours while at the same time providing much larger quantities than the traditional synthesis route. Just briefly, the mechanochemical synthesis method is based on the chemical reactions and structural changes induced by mechanical energy between metal balls and the precursors. The main challenge, however, is the rotation speed of the mill, which should be high enough so it can cause larger friction forces. Other requirements include the material and size of the metal balls, and the size of the precursors (usually nanopowders are preferred due to shorter diffusion paths). Furthermore, I have worked inhouse with yet another synthesis method, i.e., the reduction based synthesis which requires heating the precurssors for a certain time under pure hydrogen atmosphere. Based on the abovementioned synthesis routes, I have already synthesised and characterised several compositions based on the cubic ABO_3 structure, among them $BaTiO_3$, $SrTiO_3$, $BaZr_{1-x}M_xO_{3-x/2}$ M = Sc, In, Y; $0.1 < x < 0.5$), with hydrogen gas reduction based technique (exposing the materials to hydrogen gas at high temperatures) and topochemical synthesis using metal hydrides (solid state route in a controlled atmosphere due to hydride precursor being used as a reducing agent). Unfortunately, synthesis based on mechanochemical reactions was unsuccessful so far due to incompatible speed of the available mills.

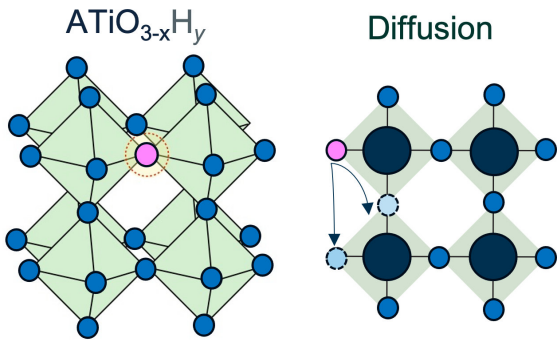

Figure 7.2: Schematic drawing of the structure and diffusion in $ATiO_3$, A= Ba, Sr, Ca etc. oxyhydrides. Note that blue circle is oxygen, pink is hydrogen, dark blue is titanium.

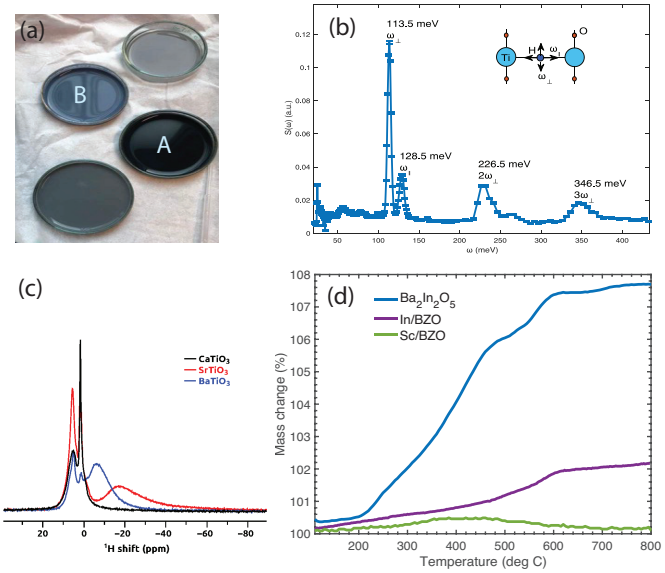

Figure 7.3: Different colors for $SrTiO_3$ (A) and $BaTiO_3$ oxyhydrides (B) (a), inelastic neutron scattering data for $BaTiO_3$, nuclear magnetic resonance data for $ATiO_3$ oxyhydrides A= Ba, Sr, and Ca, and TGA data for several newly designed oxyhydrides (d).

To this end, QENS and INS experiments as well as characterisation with NMR and TGA on a series of $BaTiO_3$, $SrTiO_3$, $BaZr_{1-x}In_xO_{3-x/2}$, $x = 0.10$ and 0.20 have been performed. For example, Figure 7.3 shows results for some of the synthesised oxyhydride such as color change upon reduction (a), vibrational modes of the hydride ions measured at IN1 at ILL (b), NMR data confirming the presence of hydride ions (c) and and TGA results confirming oxidation of the materials. The overall aim has been to test new synthesis methods and develop new class of perovskite-based and brownmillerite-based oxyhydrides which could be then further used for studies of the localised dynamics of the hydride ion by neutron scattering techniques.

Another idea was to transform the superconductor yttrium barium copper oxide, one the most studied material from a superconductivity point of view, into an oxyhydride [125, 126]. And while superconductivity *per se* is one of the hottest field nowadays, [127–129] and in particular now when we were perhaps on the verge of having superconductivity at room temperature, [130] we want to impose yet another interesting question, that is, *can we introduce hydrogen in this structure?*

For the remaining years of my PhD journey, I will shift my focus to oxyhydride perovskites and similar structures with focus on developing new materials, elucidating the hydride diffusion and optimizing the synthesis routs in hope to contribute to discovering and optimizing the newest class of materials for future energy applications. Hopefully, this can also result with collaborations between our group and leading synthesis groups in the field of oxyhydrides and other next-generation materials.

Appendix A

Fuel cells– brief considerations

A fuel cell is composed of two electrodes (cathode and anode) at each side of an eletrolyte, i.e. an ion-conducting material, in the middle that transports ions from one electrode to the other, as seen in Figure 7.4. The anode is fed with fuel (for instance hydrogen), whereas the cathode is supplied with oxidant, most commonly air. The primarily chemical reaction which undergoes within is the following: $2H_2 + O_2 = 2H_2O$.

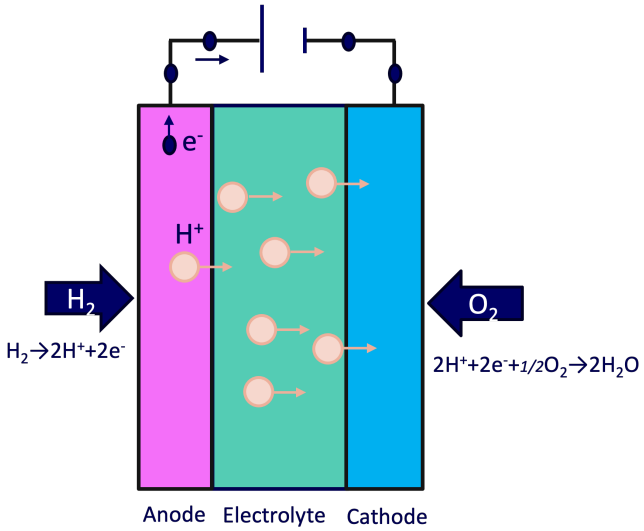

Figure 7.4: Schematic drawing of a fuel cell.

Typically, the electrolyte material is used for defining the type of the fuel cell such as fuel cells based on proton conducting electrolytes, fuel cells based on a solid acid electrolyte, and fuel cells based on proton conducting oxides. The main requirements for each component in fuel cells are given in Table 7.1.

For SOFC, the electrolyte is typically oxide-ion conducting oxide. The main advantage for SOFCs is that they can operate with different fuels, are resistant to CO and H_2S poisoning and do not require expensive materials for their electrodes (for instance noble metals), however, their disadvantage is their high operational temperature between 600–1000 °C, which is associated with higher costs and durability problems. Nowadays research in the field of SOFC, is therefore focused on development of materials manifesting high proton conductivity (ca. 10^{-2} S/cm) [31] at the low

Table 7.1: Requirements of each component. Adapted from [131].

Component	Properties	Description
Anode	• Electronic conductivity • Thermal expansion coefficient • Chemical compatibility • Electrochemical activity • Structural	• Conduct electrons from oxidation of fuel • Compatible with the other components • No reaction with electrolyte • High electrocatalytic activity with fuel gas oxidation • Porous structure to increase catalytic activity of fuel and reactant gases
Cathode	• Roles in cells • Electronic conductivity and stability	• Distribution of current related to oxygen reduction reaction which produces oxide ions • High catalytic activity for oxygen reduction and compatibility with other components
Electrolyte	• High conductivity (oxide or proton ion) • Electronic conductivity • Chemical stability	• Low electronic conductivity results in oxygen leakage and low voltage loss • Stability in air, fuel and redox reaction • Low material and fabrication cost

temperature range up to 700 °C, but despite all efforts, a suitable candidate matching this criteria has not been observed so far.

Appendix B

Incorporation of protons and mechanism of proton mobility in proton conducting oxides

Protons do not exist ipso facto in the oxide materials, but rather are incorporated into the structure [23]. The crucial requirement for proton incorporation, however, is the presence of oxygen vacancies in the structure. Oxygen vacancies can be part of the structure of these oxides (or structural defects) or can be created by acceptor doping (or impurity defects) due to the difference in valency between the transition metal and dopant atom. The procedure used for incorporation of protons in the oxygen-deficient structures is called hydration and is performed by exposing the oxide to water vapour for certain amount of time. Upon hydration, the oxygen vacancies are filled due to water dissociation, or in terms of Kröger-Vink nomenclature:

$$H_2O + V_O^{\cdot\cdot} + O_o^x = 2OH^{\cdot} \tag{7.1}$$

Where $V_O^{\cdot\cdot}$ is the oxygen vacancy present within the structure or created by acceptor doping, O_o^x is the oxygen ion on the lattice site and $OH^{\cdot}$ is the proton localized on the oxygen ion.

For the acceptor doped perovskite oxides, the number of proton concentration is roughly estimated to be equal to the dopant concentration, and once hydrated remains stable at room temperature. However, increasing the temperature above certain point results in dehydration (protons leaving the structure) due to the exothermic nature of the hydration process.

For the oxides with structural oxygen vacancies, on the other hand, the oxygen vacancies are in fact ionised defects, and therefore it can be considered that the proton concentration is proportional to the water pressure $p\mathrm{H_2O}$, whereas in the case of dominating oxygen vacancies concentration, $[\mathrm{OH}_o^{\cdot}]$ $\sim \mathrm{p}H_2\mathrm{O}$ can be used for estimation of proton concentration. It should be likewise noted that when the oxide is fully hydrated, or all oxygen vacancies are filled, the proton-determined properties no longer depend on $p\mathrm{H_2O}$ [33].

Mechanism of proton mobility in proton conducting oxides

The proton, *perse*, can be considered as infinitely small point charge which has a strong effect on the polarization of the environment, and is ultimately attracted to the electron cloud of the oxide ion; [23] however, since it interacts and associates with the neighbouring oxide ion, it can be considered a hydroxyl ion on a oxide site which moves between nearest neighbouring oxide ions. It is important to note that the hydroxyl ion OH^- is much stronger than the covalent O–H bond that is formed, and that the oxygen interaction with the oxide lattice is much stronger than the

one of the proton which results in diffusion of the proton as a single particle. The proton follows the Grotthuss-type mechanism, schematically presented in Fig 7.5 when migrating between oxide ions, with two fundamental steps taking place, i.e., proton transfers (jumps) between neighbouring oxygens and/or reorientational motion of the hydroxide group along one oxygen. Series of these localised steps result in long-range diffusion.

Figure 7.5: Schematic drawing of the Grotthuss mechanism.

The reorientation step is faster and more energetically favourable process characterised with low activation energies usually up to 0.1 eV, since it doesn't require breaking of the O–H bond [132]. Proton jumps, on the other hand, require breaking of the O–H bond, which requires additional energy which increases the activation energy of the process to up to 0.5 eV [132]. Nevertheless, proton mobility is significantly influenced and dependent on the bond between the proton and the oxygen ion. As proton jumps are influenced by the oxygen-ion fluctation, and therefore the oxygen sublattice, the transfer rate is dependent on the vibrations of oxygen ions in the structure [33, 133–135].The fluctuation of the O–O bond length (oxygen ions vibration) is decreasing the energy barrier and therefore is crucial for proton mobility. Accordingly, the growing of the O–O bond contributes to greater probability for the reorientation process [33, 133–135].

Experimental and theoretical studies encompassing proton dynamics in proton conducting oxides has been extensively studied primarily for undoped and doped perovskite type oxides [12, 70, 71, 73–77, 83, 121, 136–143]. However, despite extensive studies on the proton mobility, which is a preferred process for proton motion and which is rate-limiting for long range diffusion is still debatable topic and not fully understood question in the field.

Acknowledgements

My greatest gratitude is to my supervisor Prof. Maths Karlsson for the contentious support and transferred knowledge over the last three years. I am thankful to my examiner Prof. Per-Anders Carlsson, my co–supervisor Prof. Per Eklund, Prof. Martin Magnuson, Dr. Arnaud Le Febvrier, and Gabriel K. Nzulu for the discussions, suggestions, advice and experiment planning. To my collaborators Dr. Adrien Pericchon, Dr. Marek Koza, Prof. Max Wolff, Prof. Fabio Piccinelli and Dr. Andreas Schaefer for the enormous help in producing the papers, and interesting discussions. To Rasmus Lavén for the great help, discussions, suggestions and advice at work (and outside work really), tack så mycket! To my group members (current and former) Lucas, Kanming, Peng, Pedram, Aymen and Laura; I am so glad I get to work with all of you. Special thank you to Prof. Christine Geers for the support (and cookies); you are a true inspiration! To Prof. Itai Panas for sharing the same enthusiasm about synthesis of new samples and the numerous discussions. To Prof. Pavleta Knutsson, Vedad and Ageo for the amazing talks and discussions. I am grateful to Prof. Ulrich Häussermann and Prof. Jekabs Grins from Stockholm University for the warm welcome, supervision, and great discussions during my stay. Also, I am super thankful to Jowan, Yu-Chin and Paolo for (kinda) adopting me during my stay in Stockholm. To Doğaç (en iyi arkadaş), Esraa (my cheerful bestie), Aida, Georgios and Yiğit; words are not enough to express my gratitude for everything. To Prof. Åke Nilsson and the Jazz group: Pierre, Charity, Lennart, Börje, John, Ásgeir, Tore; I am so thankful for all of the jazz concerts and great discussions. To my food science buddies Eye, Joao, Elahe, Preceous; thank you for all those fun times, and amazing "dinner and party" hangouts. To the Dr. Genie group and Maria Saline for leading Chalmers towards more equality and inclusion. I am very thankful to the GGI girls and my Amal, Moufida and Samia for the amazing girls nights and super cool Firday nights. To my EYE mates Paul, Dominik and Samrudhi; thank you for everything. Big thanks to Oskar for making all neutron courses and conferences so fun (hvala brate). To Ruslan, Andrea, Rui, Denis, Alex, Reddy, Hampus, and Vincent for the amazing time at/outside work. I am extremely thankful to Gjoko, Anita, Mimi, Eli and Mario for all the support and guidance in Göteborg. To Dávid; köszönöm az immár közel egy évtizede nyújtott támogatást és bátorítást. To Olle ᚴᛁᛗᛒᛚᛖ ᚻᛅᚴᛁᛗᛅᚴᛁ ᛏᛁᛚᛚ. I am beyond grateful to my childhood friends (and sisters) Marija, Anika and Milena; my life wouldn't be complete without you in it! My ultimate appreciation goes to my parents Ina & Bobby. Ви благодарам за сета љубов и поддршка! Ве сакам најмногу!

CHAPTER 8

Bibliography

[1] M. K. G. Deshmukh, M. Sameeroddin, D. Abdul and M. A. Sattar, *Materials Today: Proceedings*, 2023, **80**, 1756–1759.

[2] M. Granovskii, I. Dincer and M. A. Rosen, *International Journal of Hydrogen Energy*, 2007, **32**, 927–931.

[3] J.-H. Wee, *Renewable and Sustainable Energy Reviews*, 2010, **14**, 735–744.

[4] K. Richardson, W. Steffen, W. Lucht, J. Bendtsen, S. E. Cornell, J. F. Donges, M. Drüke, I. Fetzer, G. Bala, W. von Bloh *et al.*, *Science Advances*, 2023, **9**, 2458.

[5] V. Dusastre, *Materials for sustainable energy: a collection of peer-reviewed research and review articles from Nature Publishing Group*, World Scientific, 2010.

[6] K. Yoshii, *Journal of Solid State Chemistry*, 2001, **159**, 204–208.

[7] K. Zhang, N. Zhu, M. Zhang, L. Wang and J. Xing, *Journal of Materials Chemistry C*, 2021, **9**, 3795–3799.

[8] K. Wu, A. Bera, C. Ma, Y. Du, Y. Yang, L. Li and T. Wu, *Physical Chemistry Chemical Physics*, 2014, **16**, 22476–22481.

[9] A. Shaula, Y. Pivak, J. Waerenborgh, P. Gaczyñski, A. Yaremchenko and V. Kharton, *Solid State Ionics*, 2006, **177**, 2923–2930.

[10] M. K. Hossain, M. C. Biswas, R. K. Chanda, M. H. Rubel, M. I. Khan and K. Hashizume, *Emergent Materials*, 2021, **4**, 999–1027.

[11] N. C. George, K. A. Denault and R. Seshadri, *Annu. Rev. Mater. Res.*, 2013, **43**, 1–21.

[12] M. Coduri, M. Karlsson and L. Malavasi, *Journal of Materials Chemistry A*, 2022, **10**, 5082–5110.

[13] C. Duan, J. Tong, M. Shang, S. Nikodemski, M. Sanders, S. Ricote, A. Almansoori and R. O'Hayre, *Science*, 2015, **349**, 1321–1326.

[14] K. Bae, D. Y. Jang, H. J. Choi, D. Kim, J. Hong, B.-K. Kim, J.-H. Lee, J.-W. Son and J. H. Shim, *Nat. Commun.*, 2017, **8**, 14553.

[15] S. Choi, C. J. Kucharczyk, Y. Liang, X. Zhang, I. Takeuchi, H.-I. Ji and S. M. Haile, *Nature Energy*, 2018, **8**, 202–210.

[16] Y. Chen, B. deGlee, Y. Tang, Z. Wang, B. Zhao, Y. Wei, L. Zhang, S. You, K. Pei, J. H. Kim, Y. Ding, P. Hu, F. F. Tao and M. Liu, *Nature Energy*, 2018, **3**, 1042–1050.

[17] K. Thabet, A. L. G. La Salle, E. Quarez and O. Joubert, *Solid Oxide-Based Electrochemical Devices*, 2020, 91–122.

[18] S. Fop, *Journal of Materials Chemistry A*, 2021, **9**, 18836–18856.

[19] web-page http://www.fuelcells.org accessed 070730.

[20] J. Zhao and X. Wang, *ACS omega*, 2022, **7**, 10483–10491.

[21] V. Sharma, P. Kumar, P. Dev and G. Pilania, *Journal of Applied Physics*, 2020, **128**, 034902.

[22] M. Karlsson, *Phys. Chem. Chem. Phys.*, 2015, **17**, 26.

[23] P. Colomban, *Proton Conductors: Solids, membranes and gels-materials and devices*, Cambridge University Press, 1992.

[24] C. T. J. Grotthuss, *Ann. Chim.*, 1806, **LVIII**, 54–74.

[25] A. I.Baranov, L. A. Shuvalov and N. M. Schagina, *JETP Lett.*, 1982, **36**, 459–462.

[26] J. Livage, *Solid State Ionics*, 1992, **50**, 307–313.

[27] G. Alberti and E. Torracca, *Journal of Inorganic and Nuclear Chemistry*, 1968, **30**, 1093–1099.

[28] T. Takahashi and H. Iwahara, *Rev. Chim. Miner.*, 1980, **17**, 243–253.

[29] M. Karlsson, *Dalton Trans.*, 2013, **42**, 317–329.

[30] M. Karlsson, in *Neutron Applications in Materials for Energy*, ed. G. J. Kearley and V. K. Peterson, Springer, 2015, ch. 9.

[31] B. C. H. Steele and A. Heinzel, *Nature*, 2001, **414**, 345–352.

[32] K. D. Kreuer, in *Perovskite Oxide for Solid Oxide Fuel Cells*, ed. T. Ishihara, Springer Science+Business Media, 2009.

[33] N. Kochetova, I. Animitsa, D. Medvedev, A. Demin and P. Tsiakaras, *Rsc Advances*, 2016, **6**, 73222–73268.

[34] P. Colomban, *Proton conductors*, Cambridge University Press, 1992.

[35] H. Iwahara, in *Proton conductors: Solids, membranes and gels - materials and devices*, ed. P. Colomban, University press, Cambridge, 1992, ch. 8.

[36] Y.-J. Gu, Z.-G. Liu, J.-H. Ouyang, F.-Y. Yan and Y. Zhou, *Electrochimica Acta*, 2013, **105**, 547–553.

[37] G. Ma, T. Shimura and H. Iwahara, *Solid State Ionics*, 1998, **110**, 103–110.

[38] G. Chiodelli, L. Malavasi, C. Tealdi, S. Barison, M. Battagliarin, L. Doubova, M. Fabrizio, C. Mortalo and R. Gerbasi, *Journal of Alloys and Compounds*, 2009, **470**, 477–485.

[39] R. V. Kumar, *Journal of alloys and compounds*, 2006, **408**, 463–467.

[40] K. D. Kreuer, S. Adams, W. Münch, A. Fuchs, U. Klock and J. Maier, *Solid State Ion.*, 2001, **145**, 295–306.

[41] Q. Zhang, H. Ni, L. Wang and F. Xiao, *ECS J. Solid State Sc.*, 2014, **4**, R23–R26.

[42] R. B. Cervera, Y. Oyama, S. Miyoshi, I. Oikawa, H. Takamura and S. Yamaguchi, *Solid State Ionics*, 2014, **264**, 1–6.

[43] W. Sun, M. Liu and W. Liu, *Advanced Energy Materials*, 2013, **3**, 1041–1050.

[44] Y. Liu, R. Ran, M. O. Tade and Z. Shao, *Journal of membrane science*, 2014, **467**, 100–108.

[45] H. Dai, *Ceramics International*, 2017, **43**, 7362–7365.

[46] A. Azad and J. Irvine, *Solid State Ionics*, 2007, **178**, 635–640.

[47] J. Bu, P. G. Jönsson and Z. Zhao, *Journal of Power Sources*, 2014, **272**, 786–793.

[48] J. Hyodo, K. Kitabayashi, K. Hoshino, Y. Okuyama and Y. Yamazaki, *Advanced Energy Materials*, 2020, **10**, 2000213.

[49] R. B. Cervera, Y. Oyama, S. Miyoshi, K. Kobayashi, T. Yagi and S. Yamaguchi, *Solid State Ionics*, 2008, **179**, 236–242.

[50] S. Tao and J. T. S. Irvine, *Adv. Mat.*, 2006, **18**, 1581.

[51] J. Tong, D. Clark, M. Hoban and R. O'Hayre, *Solid State Ionics*, 2010, **181**, 496–503.

[52] G. B. Zhang and S. D. M., *Solid State Ionics*, 1995, **82**, 153.

[53] G. Zhang and D. Smyth, *Solid State Ionics*, 1995, **82**, 153–160.

[54] A. Jarry, E. Quarez, K. Kravchyk and O. Joubert, *Solid State Ionics*, 2012, **216**, 11–14.

[55] M. B. Hanif, S. Rauf, M. Motola, Z. U. D. Babar, C.-J. Li and C.-X. Li, *Materials Research Bulletin*, 2022, **146**, 111612.

[56] K. D. Kreuer, *ChemPhysChem*, 2002, **3**, 771–775.

[57] T. Yakima, K. Koide, H. Take, N. Fukatsu and H. Iwahara, *Solid State Ionics*, 1995, **79**, 333–337.

[58] G. Marnellos and M. Stoukides, *Science*, 1998, **282**, 95–98.

[59] H. Malerød-Fjeld, D. Clark, I. Yuste-Tirados, R. Zanón, D. Catalán-Martinez, D. Beeaff, S. H. Morejudo, P. K. Vetre, T. Norby, R. Haugsrud, J. M. Serra and C. Kjølseth, *Nature Energy*, 2017, **2**, 923–931.

[60] S. H. Morejudo, R. Zanón, S. Escolástico, I. Yuste-Tirados, H. Malerød-Fjeld, P. K. Vestre, W. G. Coors, A. Martinez, T. Norby, J. M. Serra and C. Kjølseth, *Science*, 2016, **353**, 563–566.

[61] D. Medvedev, J. Lyagaeva, E. Gorbova, A. Demin and P. Tsiakaras, *Progress in Materials Science*, 2016, **75**, 38–79.

[62] J. Bu, P. G. Jönsson and Z. Zhao, *Ceramics International*, 2015, **41**, 2558–2564.

[63] C. Duan, R. Kee, H. Zhu, N. Sullivan, L. Shu, L. Bian, D. Jennings and R. O'Hayre, *Nature Energy*, 2019, **4**, 230–240.

[64] J. Habash, J. Raftery, R. Nuttall, H. Price, C. Wilkinson, A. Kalb and J. Helliwell, *Acta Crystallogr. D*, 2000, **56**, 541–550.

[65] F. Iguchi, T. Tsurui, N. Sata, Y. Nagao and H. Yugami, *Solid State Ionics*, 2009, **180**, 563–568.

[66] D. Navas, S. Fuentes, A. Castro-Alvarez and E. Chavez-Angel, *Gels*, 2021, **7**, 275.

[67] G. K. Zulu, E. Naumovska, M. Karlsson, P. Eklund, M. Magnusson and A. le Febvrier, *Submitted*, 2022.

[68] A. Baptista, F. Silva, J. Porteiro, J. Míguez and G. Pinto, *Coatings*, 2018, **8**, 402.

[69] D. Noferini, M. M. Koza, S. M. H. Rahman, Z. Evenson, G. J. Nilsen, S. Eriksson, A. R. Wildes and M. Karlsson, *Phys. Chem. Chem. Phys.*, 2018, **20**, 13697–13704.

[70] P. Du, Q. Chen, Z. Fan, H. Pan, F. G. Haibach, M. A. Gomez and A. Braun, *Communications Physics*, 2020, **3**, 200:1–9.

[71] W. Münch, G. Seifert, K. D. Kreuer and J. Maier, *Solid State Ion.*, 1996, **86-88**, 647–652.

[72] M. Karlsson, *Phys. Chem. Chem. Phys.*, 2015, **17**, 26–38.

[73] R. Hempelmann, C. Karmonik, T. Matzke, M. Cappadonia, U. Stimming, T. Springer and M. A. Adams, *Solid State Ion.*, 1995, **77**, 152–156.

[74] T. Matzke, U. Stimming, C. Karmonik, M. Soetramo, R. Hempelmann and F. Güthoff, *Solid State Ion.*, 1996, **86-88**, 621–628.

[75] C. Karmonik, R. Hempelmann, J. Cook and F. Güthoff, *Ionics*, 1996, **2**, 69.

[76] D. Noferini, M. M. Koza and M. Karlsson, *J. Phys. Chem. C*, 2017, **121**, 7088–7093.

[77] D. Noferini, M. M. Koza, S. M. H. Rahma, Z. Evenson, G. J. Nilsen, S. Eriksson, A. R. Wildes and M. Karlsson, *Phys. Chem. Chem. Phys.*, 2018, **20**, 13697–13704.

[78] M. Pionke, T. Mono, W. Schweika, T. Springer and H. Schober, *Solid State Ion.*, 1997, **97**, 497–504.

[79] M. Karlsson, D. Engberg, M. E. Björketun, A. Matic, G. Wahnström, P. G. Sundell, P. Berastegui, I. Ahmed, P. Falus, B. Farago, L. Börjesson and S. Eriksson, *Chem. Mater.*, 2010, **22**, 740–742.

[80] D.-H. Kim, B.-K. Kim and Y.-C. Kim, *Solid State Ion.*, 2013, **213**, 18–21.

[81] M. A. Gomez, M. A. G. A. S. Jindal, K. D. Rule and V. R. Cooper, *Journal of Chemical Physics*, 2005, **123**, 094703.

[82] M. Karlsson, M. E. Björketun, P. G. Sundell, A. Matic, G. Wahnström, D. Engberg, L. Börjesson, I. Ahmed, S. G. Eriksson and P. Berastegui, *Phys. Rev. B*, 2005, **72**, 094303: 1–7.

[83] L. Mazzei, A. Perrichon, A. Mancini, L. Malavasi, S. F. Parker, L. Börjesson and M. Karlsson, *J. Phys. Chem. C*, 2019, **123**, 26065–26072.

[84] K. D. Kreuer, S. J. Paddison, E. Spohr and M. Schuster, *Chem. Rev.*, 2004, **104**, 4637–4678.

[85] M. Cherry, M. S. Islam, J. D. Gale and C. R. A. Catlow, *Solid State Ion.*, 1995, **77**, 207–209.

[86] L. Malavasi, C. A. J. Fisher and M. S. Islam, *Chem. Soc. Rev.*, 2010, **39**, 4370.

[87] J. Bielecki, S. F. Parker, L. Mazzei, L. Börjesson and M. Karlsson, *J. Mater. Chem. A*, 2016, **4**, 1224–1232.

[88] A. Perrichon, M. Jiminez-Ruiz, L. Mazzei, S. M. H. Rahman and M. Karlsson, *J. Mater. Chem. A*, 2019, **7**, 17626–17636.

[89] N. Preux, A. Rolle and R. Vannier, in *Functional materials for sustainable energy applications*, Elsevier, 2012, pp. 370–401.

[90] A. Perrichon, M. M. Koza, Z. Evenson, B. Frick, F. Demmel, P. Fouquet and M. Karlsson, *Chemistry of Materials*, 2023.

[91] A. Mancini, J. F. Shin, A. Orera, P. R. Slater, C. Tealdi, Y. Ren, K. L. Page and L. Malavasi, *Dalton Trans.*, 2012, **41**, 50–53.

[92] J. F. Shin, A. Orera, D. Apperley and P. Slater, *Journal of Materials Chemistry*, 2011, **21**, 874–879.

[93] J. Bielecki, S. F. Parker, D. Ekanayake, S. M. H. Rahman, L. Börjesson and M. Karlsson, *J. Mater. Chem. A*, 2014, 16915–16924.

[94] J.-R. Martinez, C. E. Mohn, S. Stoelen and N. L. Allan, *J. Solid State Chem.*, 2007, **180**, 3388.

[95] V. Jayaraman, A. Magrez, M. Caldes, O. Joubert, F. Taulelle, J. Rodriguez-Carvajal, Y. Piffard and L. Brohan, *Solid State Ionics*, 2004, **170**, 25.

[96] E. T. Sayed, A. G. Olabi, A. H. Alami, A. Radwan, A. Mdallal, A. Rezk and M. A. Abdelkareem, *Energies*, 2023, **16**, 1415.

[97] R. Pynn, *Neutron Scattering - A Primer*, 2000.

[98] R. Hempelmann, *Quasielastic neutron scattering and solid state diffusion*, 2000.

[99] R. Lavén, *Dynamical properties of metal halide and oxyhydride perovskites*, 2023.

[100] M. Karlsson, A. Matic, D. Engberg, M. E. Björketun, M. M. Koza, I. Ahmed, G. Wahnström, P. Berastegui, L. Börjesson and S. G. Eriksson, *Solid State Ion.*, 2009, **180**, 22.

[101] D. Noferini, M. M. Koza, P. Fouquet, G. J. Nilsen, M. C. Kemei, S. M. H. Rahman, M. Maccarini, S. Eriksson and M. Karlsson, *J. Phys. Chem. C*, 2016, **120**, 13963–13969.

[102] P. Sindhu, *Fundamentals of Molecular Spectroscopy.*, New Age International, 2006.

[103] S. Gaisford, V. Kett and P. Haines, *Principles of thermal analysis and calorimetry*, Royal society of chemistry, 2019.

[104] E. Fabbri, D. Pergolesi and E. Traversa, *Chem. Soc. Rev.*, 2010, **39**, 4355.

[105] A. K. E. Eriksson, S. M. Selbach, C. S. Knee and T. Grande, *Journal of American Ceramic Society*, 2014, **07**, 2654–2661.

[106] C. W. Mburu, S. M. Gaita, C. S. Knee, M. J. Gatari and M. Karlsson, *J. Phys. Chem. C*, 2017, **121**, 16174–16181.

[107] M. Wilde and K. Fukutani, *Surface science reports*, 2014, **69**, 196–295.

[108] L. Mazzei, M. Wolff, D. Pergolesi, J. A. Dura, L. Börjesson, P. Gutfreund, M. Bettinelli, T. Lippert and M. Karlsson, *J. Phys. Chem. C*, 2016, **120**, 28415–28422.

[109] E. Mamontov and K. W. Herwig, *Rev. Sci. Instrum.*, 2011, **82**, 085109.

[110] M. Karlsson, *Solid state proton conductors: hydrated perovskites and hydrated alkali thiohydroxogermanates*, Chalmers University of Technology, 2007.

[111] W. Lohstroh and Z. Evenson, *Journal of large-scale research facilities JLSRF*, 2015, **1**, A15–A15.

[112] A. Perrichon, *Ph.D. thesis*, Université de Montpellier, 2015.

[113] M. Karlsson, *Solid state proton conductors: hydrated perovskites and hydrated alkali thiohydroxogermanates*, Chalmers University of Technology, 2007.

[114] C. Eklöf-Österberg, *Structure-dynamics relationships in perovskite oxyhydrides and alkali silanides*, Chalmers Tekniska Hogskola (Sweden), 2019.

[115] L. Mazzei, A. Perrichon, A. Mancini, L. Malavasi, S. F. Parker, L. Börjesson and M. Karlsson, *J. Phys. Chem. C*, 2019, **123**, 26065–26072.

[116] M. Weller and N. Young, 2017.

[117] F. Demmel, *Quasielastic Neutron Scattering*, 2013, `https://www.isis.stfc.ac.uk/Pages/quasi-elastic-neutron-scattering13583.pdf`.

[118] M. Karlsson, A. Matic, D. Engberg, M. E. Björketun, M. M. Koza, I. Ahmed, G. Wahnström, L. Börjesson and S.-G. Eriksson, *Solid State Ionics*, 2009, **180**, 22–28.

[119] K. D. Kreuer, A. Fuchs and J. Maier, *Solid State Ion.*, 1995, **77**, 157–162.

[120] L. Mazzei, F. Piccinelli, M. Bettinelli, S. F. Parker and M. Karlsson, *Solid State Ionics*, 2021, **365**, 115624.

[121] L. Mazzei, A. Perrichon, A. Mancini, G. Wahnström, L. Malavasi, S. F. Parker and L. Börjesson, *J. Mater. Chem. A*, 2019, **7**, 7360–7372.

[122] M. Karlsson, I. Ahmed, A. Matic and S. G. Eriksson, *Solid State Ion.*, 2008.

[123] L. Mazzei, D. Rukser, F. Biebl, B. Grimm-Lebsanft, G. Neuber, D. Pergolesi, L. Börjesson, M. Rübhausen, J. Andreasson and M. Karlsson, *Journal of physics. Condensed Matter: an Institute of Physics Journal*, 2020, **32**, 405403–405403.

[124] H. Kageyama, K. Hayashi, K. Maeda, J. P. Attfield, Z. Hiroi, J. M. Rondinelli and K. R. Poeppelmeier, *Nature Commun.*, 2018, **9**, 772.

[125] A. A. Abdul Hussein, A. M. Abdul Hussein and N. A. Hasan, *Journal of Applied Sciences and Nanotechnology*, 2023, **3**, 65–79.

[126] P. Cayado, J. Hänisch, K. Iida and C. Senatore, *Superconductor Science and Technology*, 2023.

[127] W. E. Pickett, *Reviews of Modern Physics*, 1989, **61**, 433.

[128] M. Mandal, N. C. Drucker, P. Siriviboon, T. Nguyen, A. Boonkird, T. N. Lamichhane, R. Okabe, A. Chotrattanapituk and M. Li, *Chemistry of Materials*, 2023.

[129] K. Jiang, T. Wu, J.-X. Yin, Z. Wang, M. Z. Hasan, S. D. Wilson, X. Chen and J. Hu, *National Science Review*, 2023, **10**, nwac199.

[130] S. Lee, J.-H. Kim and Y.-W. Kwon, *arXiv preprint arXiv:2307.12008*, 2023.

[131] Y. Gao, M. Zhang, M. Fu, W. Hu, H. Tong and Z. Tao, *Energy Reviews*, 2023, 100038.

[132] K. D. Kreuer, *Solid State Ion.*, 2000, **136-137**, 149–160.

[133] K.-D. Kreuer, *Journal of Molecular Structure*, 1988, **177**, 265–276.

[134] K. D. Kreuer, *Chem. Mater.*, 1996, **8**, 610–641.

[135] M. S. Islam, R. A. Davies and J. D. Gale, *Chemical Communications*, 2001, 661–662.

[136] M. E. Björketun, P. G. Sundell and G. Wahnström, *Faraday Discuss.*, 2007, **134**, 247–265.

[137] P. G. Sundell, M. E. Björketun and G. Wahnström, *Phys. Rev. B: Condens. Matter*, 2007, **76**, 094301.

[138] P. Raiteri, J. D. Gale and G. Bussi, *J. Phys. Condens. Matter*, 2011, **23**, 334213.

[139] N. Kitamura, J. Akola, S. Kohara, K. Fujimoto and Y. Idemoto, *J. Phys. Chem. C.*, 2014, **118**, 140725075203008.

[140] R. Hempelmann, M. Soetratmo, O. Hartmann and R. Wäppling, *Solid State Ion.*, 1998, **107**, 269–280.

[141] E. J. Spahr, L. Wen, M. Stavola, L. A. Boatner, L. C. Feldman, H. H. Tolk and G. Lüpke, *Phys. Rev. Lett.*, 2010, **104**, 205901.

[142] A. Braun and Q. Chen, *Nature Communications*, 2017, **8**, 15830:1–8.

[143] Q. Chen, Y.-W. Huang, M. Baldini, A. Hushur, V. Pomjakushin, S. Clark, W. L. Mao, M. H. Manghnani, A. Braun and T. Graule, *J. Phys. Chem. C*, 2011, **115**, 24201–24027.